

1  
2      **Single- and Multi-Pass Magnetometric Subsurface Ocean Detection and**  
3      **Characterization in Icy Worlds Using Principal Component Analysis (PCA):**  
4      **Application to Triton**  
5

6      **C. J. Cochrane<sup>1</sup>, R. R. Persinger<sup>2</sup>, S. D. Vance<sup>1</sup>, E. L. Midkiff<sup>1</sup>, J. Castillo-Rogez<sup>1</sup>,**  
7      **A. Luspay-Kuti<sup>3</sup>, L. Liuzzo<sup>4</sup>, C. Paty<sup>5</sup>, K. L. Mitchell<sup>1</sup>, L. M. Prockter<sup>3</sup>**

8  
9      <sup>1</sup>Jet Propulsion Laboratory, California Institute of Technology

10      <sup>2</sup>Aerospace Corporation

11      <sup>3</sup>John Hopkins University Applied Physics Laboratory

12      <sup>4</sup>Space Sciences Laboratory, University of California, Berkeley

13      <sup>5</sup>University of Oregon

14  
15      Corresponding author: Corey J. Cochrane ([corey.j.cochrane@jpl.nasa.gov](mailto:corey.j.cochrane@jpl.nasa.gov))

16  
17      **Key Points:**

- 18      • A novel sub-surface ocean detection and characterization method has been developed  
19      based on PCA processing of magnetic induction data
- 20      • Enables differentiation between ocean-plus-ionosphere and ionosphere-only induction  
21      responses in the presence of various noise sources
- 22      • Applied here to the compelling target of Triton, thought to possibly harbor a sub-surface  
23      ocean beneath a highly conducting ionosphere

**28 Abstract**

29 Many moons in the solar system are thought to potentially harbor hidden oceans based on the  
30 features observed at their surfaces. However, the magnetic induction signatures measured in the  
31 vicinity of these moons provide the most compelling evidence for the presence of a subsurface  
32 ocean, specifically for the Jovian moons Europa and Callisto. Interpretation of these magnetic  
33 signatures can be convoluted due to the various systematic and random sources of noise that are  
34 present in the magnetic field measurement. In this work, a novel magnetometric ocean detection  
35 methodology based on Principal Component Analysis (PCA) is presented and shown to provide  
36 enhanced discrimination and geophysical characterization of ocean properties in the presence of  
37 noise and error sources. The proposed methodology is robust for a single-encounter mission or  
38 an orbiting mission with multiple flybys. Here, it is applied to the Neptunian moon Triton as a  
39 prime example of an active, potential ocean world residing in the requisite time-varying  
40 magnetic field environment that enables magnetic induction investigation of its interior. In  
41 addition to the usual noise sources, other confounding factors are addressed, including the  
42 presence of an intense conductive ionosphere, the small amplitude of Neptune's driving  
43 magnetic field, and the uncertainty of Neptune's magnetic phase at the time-of-arrival which can  
44 potentially hinder accurate ocean detection and characterization. The proposed methodology is  
45 applicable to any moon in the solar system residing in a time-varying magnetic field  
46 environment.

47

**48 Plain Language Summary**

49 The search for habitable oceans in the solar system motivates the need for advances in analytic  
50 techniques to positively determine the presence of subsurface oceans in challenging  
51 environments. The Principal Component Analysis (PCA) analysis method described in this paper  
52 is a new paradigm for processing space-based magnetic field measurements for definitive  
53 detection and constrained characterization of subsurface oceans. Using Neptune's largest moon  
54 Triton as an example ocean world, PCA is directly applied to a three-axis magnetic field dataset  
55 and shown to be a powerful ocean classification tool for a single or multiple flybys, even in the  
56 presence of Triton's highly conducting ionosphere which can mask the magnetic response from  
57 the ocean. The method is able to reliably distinguish between the magnetic field signatures  
58 associated with the ocean-plus-ionosphere and ionosphere-only model classes and can further  
59 determine key characteristics of the hidden ocean in the face of the confounding factors of a  
60 conductive ionosphere, local plasma current perturbations, spacecraft timing and position  
61 uncertainties, data outages, and various sources of instrument noise. The flexibility and  
62 extensibility afforded by the PCA-based method enhance the existing and future capabilities for  
63 ocean detection and characterization at candidate ocean worlds throughout the solar system.

64

65

66

67

68

## 69    1 Introduction

70  
 71 Many worlds exist in the solar system with salty subsurface liquid-water oceans beneath icy crusts, facilitated by  
 72 surface tidal and librational heating. Saturn's moons Enceladus and Titan are known to be water-ocean worlds.  
 73 Enceladus exhibits impressive jets of water vapor that spray from fissures in the south pole region (Porco et al.  
 74 2006), likely the result of tidally-driven fault-motion heating of water sourced from a global or regional subsurface  
 75 ocean below a thick ice shell (Nimmo et al. 2007). Time-varying magnetic induction signatures measured by  
 76 Galileo's magnetometers in the vicinity of Jupiter's moons Europa and Callisto suggest these bodies also have salty  
 77 liquid-water oceans beneath their surfaces (Khurana et al. 1998, Kivelson et al. 1999), while recent Hubble  
 78 investigations indicate a large underground water ocean at Ganymede (Saur et al. 2015). Although limited data  
 79 exists, many moons of the gas giants are thought to possibly contain hidden oceans. The five large Uranian moons  
 80 (Miranda, Ariel, Umbriel, Titania, and Oberon) all in some form exhibit surface features consistent with a  
 81 subsurface liquid ocean (e.g., Croft and Soderblom 1991, Schenk et al., 2020), and also reside in a time-varying  
 82 magnetic environment which enables magnetic induction detection (Arridge and Egginton 2021, Cochrane et al.,  
 83 2021, Weiss et al., 2021). Neptune's moon Triton, the focus of this paper, is a particularly compelling mission target  
 84 with numerous characteristics consistent with the presence of a subsurface ocean. Tidal heating from a highly  
 85 inclined retrograde orbit, evidence of cryovolcanic activity, active plumes, and unusual geological features imaged  
 86 by Voyager 2 suggest the possibility of a liquid layer beneath the surface (Croft et al. 1995, Nimmo et al. 2016). The  
 87 Outer Planets Assessment Group (OPAG) Roadmap to Ocean Worlds (Hendrix et al. 2019) states that "*Triton is the*  
 88 *highest priority ocean world ... to target in the near term.*"

89  
 90 Spacecraft equipped with a 3-axis magnetometer have been able to confirm that some of these moons are indeed  
 91 ocean worlds based on the magnetic induction signatures measured near their surfaces, Europa and Callisto being  
 92 the prime examples. In this work, a novel ocean detection methodology based on Principal Component Analysis  
 93 (PCA) is used to directly process the magnetic induction fields measured by a magnetometer, significantly  
 94 increasing positive discrimination and geophysical characterization of a subsurface ocean in the presence of various  
 95 noise and magnetic error sources. The proposed methodology is shown to be robust for a single-pass encounter or a  
 96 multi-pass orbiting mission at a variety of other possible ocean worlds including the moons of Uranus or Jupiter,  
 97 each with a unique magnetospheric environment. In this work, the following key concepts are presented: ocean  
 98 induced magnetic moments, scaled induced magnetic moments, magnetic separation of *ocean* and *no-ocean* classes,  
 99 and the influence of the spacecraft trajectory through a moon's induction fields. Also presented is the method's  
 100 sensitivity to instrument parameters (sample-rate, noise, and offsets), spacecraft uncertainties (position, attitude, and  
 101 timing), and anticipated plasma currents. Prior to presenting PCA's applicability to ocean detection and  
 102 characterization, an independent closed form analytical verification of the methodology based on discrete-time  
 103 signal energy preservation of the magnetic field time-series is described. Finally, PCA's transformation of the high-  
 104 dimensional magnetic field time-series into a reduced, visually convenient, 3-dimensional scaled magnetic moment  
 105 ocean classification space and the resulting ability to clearly distinguish the presence of a conductive liquid layer are  
 106 illustrated.

## 107    2 Subsurface Ocean Detection using Magnetometric Data

### 108    2.1 The Favorable Magnetic Environment at Triton

109 The phenomenon of magnetic induction occurs when a time-varying magnetic field induces electrical eddy currents  
 110 within a conducting medium such as a subsurface salty ocean, which in turn generates a secondary induced magnetic  
 111 field that can be remotely sensed by a magnetometer. Neptune's largest moon Triton represents a potential ocean  
 112 world of high interest to the science community (Hansen et al., 2021, Hendrix et al. 2019). It is immersed in  
 113 Neptune's strong time-varying magnetic field, which facilitates magnetic induction investigation of its interior.

114  
 115 Neptune's unusual magnetic field has a large magnetic moment ( $13,300 \text{ nT}\cdot\text{R}_N^3$  or  $2.2 \times 10^{17} \text{ T}\cdot\text{m}^3$ , roughly 27 times  
 116 that of Earth's), with a magnetic pole tilted  $47^\circ$  with respect to Neptune's spin axis and shifted by  $0.55 \text{ R}_N$  from  
 117 Neptune's center (Connerney et al., 1991). The spin axis is tilted  $28^\circ$  with respect to the normal of the ecliptic plane,  
 118 and Triton's retrograde orbit is a steeply inclined  $157^\circ$  relative to Neptune's equator. As a result of this complicated  
 119 geometry, Triton experiences cyclic variations in Neptune's driving field at two fundamental periods: the synodic  
 120 period of Neptune's rotation (~14 hours) and Triton's own orbital period (~141 hours) (Saur et al. 2010). Harmonics

121 and beat frequencies between these two fundamental periods are lower in amplitude but still provide measurable ( $> 1\text{nT}$ ) contributions to the total external driving fields.  
 122  
 123

124 The periodic variation in the magnetic field at Triton as it cyclically traverses Neptune's magnetic latitudes critically  
 125 enables magnetometric ocean detection. A fortuitous additional advantage of this orbital configuration is that Triton  
 126 spends minimal time within a couple of planetary radii ( $< 2 R_N$ ) of Neptune's magnetic equator, where plasma  
 127 effects are anticipated to be at their largest and roughly confined to a sheet that corotates with the planet (Mejnerten  
 128 et al. 2016). Moreover, when Triton does interact with the plasma sheet, particle densities are expected to be very  
 129 low at Triton's significant distance from Neptune ( $14 R_N$ ), measured at  $0.003 \text{ /cm}^3$  by Voyager 2 (Zhang et al. 1991)  
 130 As a result, induced fields from plasma currents minimally perturb the local magnetic field around Triton (Liuzzo et  
 131 al. 2021).  
 132

133 However, the surprisingly intense ionosphere of Triton presents a potential confounding factor, because induced  
 134 electrical currents in the ionosphere generate a secondary magnetic field which could mask an induction response  
 135 originating from an ocean (Hartkorn & Saur 2017). Radio occultation measurements made by Voyager 2 found peak  
 136 electron concentrations of  $2.3\text{--}4.6 \times 10^4 \text{ cm}^{-3}$  (Tyler 1989). This signal is significantly higher than can be attributed  
 137 to solar UV which suggests precipitation of charged particles from Neptune's magnetosphere (Sittler et al. 1996, Ip  
 138 1990, Strobel 1990, Yung 1990, Mandt 2019). Another concern is that at Triton's orbital distance, the strength of  
 139 Neptune's driving field is reduced to levels well below those encountered at the Jovian moons, complicating ocean  
 140 detection when accounting for potential sources of measurement error and systemic noise. Additionally, because of  
 141 Neptune's gaseous outer layer, its core rotation period – and therefore the phase of the synodic (14 hour) magnetic  
 142 wave – will remain unknown until arrival at the Neptune system. An ocean detection method for a single flyby of  
 143 Triton must be able to distinguish between ocean and ionosphere induction signals for any magnetic phase of the  
 144 synodic period.  
 145

## 146 2.2 New Approach for Subsurface Detection

147 The conventional approach to detecting a conductive subsurface ocean is least-squares inversion of the magnetic  
 148 induction field time-series measured by a magnetometer, making use of the spacecraft's trajectory and the dipole  
 149 field equation (see Kivelson (2002) and Schilling (2004) for related inversion schemes). For a single flyby of a  
 150 particular moon, a data inversion step can be used on the three-channel magnetometer data to yield the three-  
 151 element total induced magnetic moment vector generated from the subsurface ocean at closest approach. This  
 152 induced magnetic moment is formed from the sum of the individual magnetic moments associated with the ocean's  
 153 response to the two primary waves (synodic and orbital), including the associated harmonics and beat frequencies of  
 154 the two fundamental periods, and provides insight into the properties of the ocean.  
 155

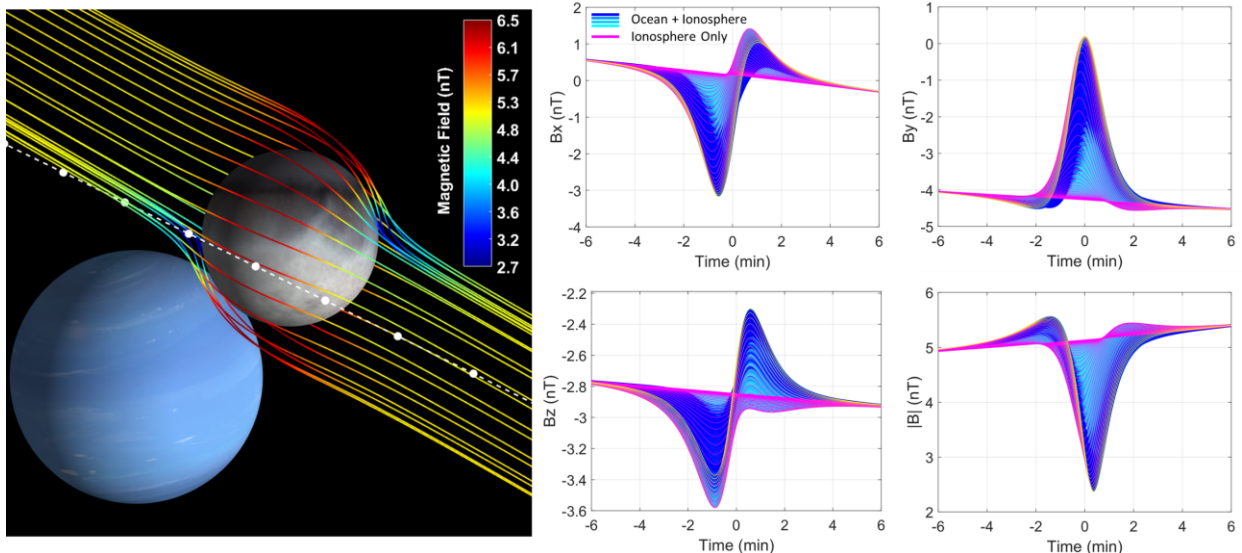
156 The novel approach described in this paper first formulates a large dataset of forward-modeled induced dipole  
 157 magnetic field time-series, generated from thousands of different potential interior models, and then processes this  
 158 data using the well-established data-dimensionality reduction technique of Principal Component Analysis (PCA).  
 159 Noisy magnetic field measurements acquired near the body of interest can then also be broken down into their  
 160 principal components (PCs) to distinguish between *ionosphere-only* and *ocean-plus-ionosphere* model classes. This  
 161 method uses all available information is used in the processing (i.e., nothing is discarded) and the retained signal  
 162 energy increases separation between model classes. At bodies like Triton where the strength of the driving magnetic  
 163 field, and hence the induced fields, are relatively small, this boost in separation reduces false positive and false  
 164 negative ocean classifications of noisy measurements.  
 165

## 166 2.3 Two Distinct Methodology Pathways

167 Subsurface ocean detection is enabled by 3-axis magnetometer measurements acquired in the vicinity of a planetary  
 168 body immersed in a time-varying magnetic field. In any realistic scenario, relatively close proximity to the body's  
 169 surface is necessary to achieve usable measurements because field strength falls off rapidly with distance from the  
 170 center of the moon (e.g.,  $1/r^3$  for a dipole response and  $1/r^4$  for a quadrupole response). Figure 1 (left) illustrates the  
 171 magnetic field lines associated with sum total of Neptune's magnetospheric field and the induction field at Triton,  
 172 color-coded according to field strength in units of nanoteslas (nT), along with an example single-pass trajectory  
 173 (white line). The data measurement interval of interest for a single flyby (velocity  $\sim 18 \text{ km/sec}$ ) spans roughly  $\pm 6$   
 174 minutes about closest approach to Triton, at a minimum altitude above the surface ( $R_T=1,353.4 \text{ km}$ ) of less than 400  
 175 km ( $r = 1,754 \text{ km}$ ).  
 176

176  
177  
178  
179  
180  
181  
182  
183  
184  
185  
186  
187  
188

To reliably ascribe the measured induced response from the combination of a conducting subsurface ocean and conducting ionosphere, an extensive set of induced magnetic field time-series is forward modeled for a wide range of plausible physical properties of Triton's known ionosphere and its potential ocean as described in Section 3.2. To cover this range of possibilities, a parameter space of more than 13,000 combinations of ocean and ionosphere characteristics is defined for this study, and the magnetic responses are computed per a multi-shell conductivity model described in more detail in Section 3.2. Figure 1 (right) depicts the anticipated measured total magnetic field over the 12-minute encounter period. The simulated magnetometer signals colored in magenta represent the ionosphere-only models and the ocean-plus-ionosphere models are represented by shades of blue. From the figure, it is obvious that the difference between the ionosphere-only (magenta) and ionosphere-plus-ocean (blue shades) model time-series is difficult to differentiate based on line shape and amplitude alone. This suggests the need for more powerful data analysis tools.

189  
190

**Figure 1:** The approach described uses forward modeling of magnetic response functions resulting from Neptune's magnetic field interacting with a wide range of proposed, plausible ionosphere and ocean properties. (left) Simulated magnetic field lines of the total magnetic field in the vicinity of Triton including Triton's induced magnetic field and Neptune's magnetic field at a time near closest approach of the moon. The white dashed line with white dots illustrates the nominal flyby trajectory used for this analysis. (right) Forward modeled magnetic field time-series evaluated along the flyby, blue indicative of ocean plus ionosphere responses and magenta of ionosphere-only responses.

191  
192  
193  
194  
195  
196  
197  
198  
199  
200  
201  
202  
203  
204  
205  
206  
207  
208  
209  
210  
211  
212  
213

Figure 2 depicts two possible paths for ocean detection; Path 1 illustrates the traditional data inversion technique (with an additional stage of magnetic moment forward modeling) and Path 2 illustrates the proposed new methodology using PCA. Both paths depend on forward modeling the total induced magnetic moments for various interior magnetic induction models which depend on the ocean and ionosphere parameter space and the driving magnetic field (15 individual magnetic waves with different frequencies were simulated) of the parent planet as described in Section 3.1. The time-varying portion of the total induced magnetic moment, evaluated at closest-approach, for each model is a 3-element vector  $[M_x, M_y, M_z]$  (see section 3.4). Only  $M_x$  and  $M_y$  of all models are plotted in the figure as they contain the most information. Ocean-plus-ionosphere (blue shades) and ionosphere-only (magenta) models are distinguished by color. It is precisely these computed quantities that serve as the magnetic moment classification space for the data inversion methodology taken in Path 1. Using the spacecraft trajectory ephemeris and the magnetic dipole field equation, Path 1 entails inverting the magnetic field measurements to obtain a representative magnetic moment that can be projected into the ocean classification space (represented by orange dot in the figure) for ocean property inference. The separation from the magenta ionosphere-only models (in units of nT) is a representation of ocean detection confidence.

Path 2 also requires the use of the forward modeled induced magnetic moments but uses them to compute the induced dipole magnetic field time-series along the spacecraft trajectory for all ionosphere-only and ocean-plus-ionosphere models. These induced magnetic field time-series are represented by  $3N$  samples ( $N$  samples for each of the three channels of the magnetometer, dictated by the sampling rate) and are directly fed into the PCA data analysis tool for dimensionality reduction (further described in Section 5). The PCs of all models that are computed in this path are defined by a 3-element vector [PC1, PC2, PC3] and can also be used as an ocean classification space (only PC1 and PC2 are shown in the block diagram). In this process, PCA computes a set of eigenvectors that are used to project the measurement (also a total of  $3N$  samples in length) into the PCA ocean classification space, again represented by the orange circle. Note that both classification spaces are characterized by units of nT. Note the large separation between the two model classes (blue and magenta) for the PCA ocean classification space.

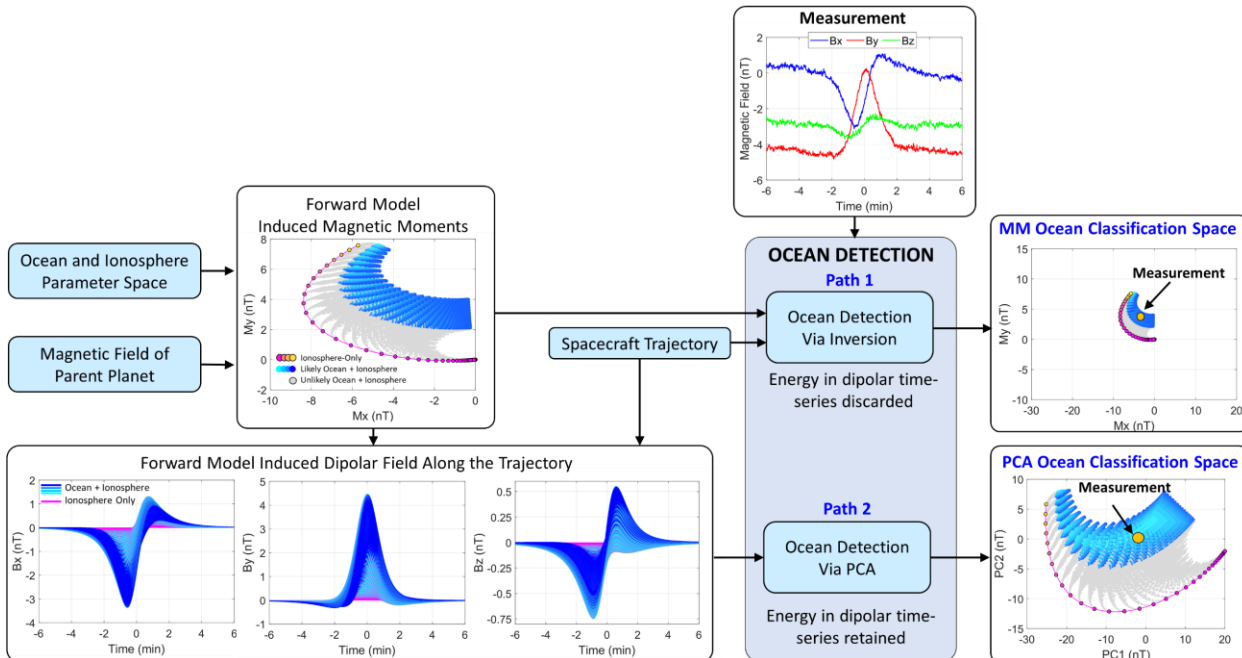


**Figure 2:** Block diagram illustrating the high-level steps that need to be performed for ocean detection using single inversion/least squares (Path 1) and the novel PCA scheme described in this paper (Path 2). Some current ocean detection approaches extend Path 1 and perform a second stage of inversion to recover individual magnetic moments for select magnetic waves of interest. Both paths provide the ability to perform ocean detection; however, the PCA path results in larger separation between the two model classes.

While PCA has been widely used for decades in a variety of data analysis applications to reveal correlations in multi-dimensional experimental data, its novel application to magnetometer measurements for ocean detection demonstrates a significant advantage by reducing the time-dimensionality of the induced dipolar magnetic field time-series into a more easily visualized 3-dimensional space in which separation between various ocean-plus-ionosphere and ionosphere-only data classes is systematically increased. Because PCA is applied directly to the magnetic field time-series acquired by the magnetometer, the computed PCs retain all signal energy owing to the orthonormality property of the eigenvectors used for the linear projection. The PCs of the models effectively represent the superposition of scaled magnetic moments. This scaling provides increased separation (relative to the magnetic moment classification space) between the two different model classes and is a direct result of the physical relationship between the dipolar fields and the magnetic moments that generate them (see Sections 3.4 and 3.5).

As the information about a moon's interior (ocean depth, thickness, and conductivity) is contained within the induced magnetic moments, both ocean detection methodology paths are generally viable based on the separability of the distinctive data models that contain oceans and ones that do not. However, for ocean detection at Triton – and for investigations of other candidate ocean worlds – ocean detection using PCA is advantageous because the *scaled total magnetic moments* increase the magnetic separation between the ionosphere-only and ionosphere-plus-ocean

249 model classes enhancing distinguishability for ocean detection purposes. By contrast, inverting for the total  
 250 magnetic moments discards signal energy, resulting in a comparatively reduced magnetic separation between data  
 251 classes.

## 252 3 Forward Modeling the Induced Magnetic Moments and Dipole 253 Response

### 254 3.1 Neptune's Magnetic Field and Plasma Sheet Geometry

255 Measurements made by *Voyager 2* in the magnetosphere of Neptune revealed that Triton resides in a highly dynamic  
 256 magnetic field environment, ideal for magnetic induction investigation into the presence of a subsurface ocean.  
 257 Neptune's magnetic field likely originates from a self-sustaining dynamo acting within a thin electrically conductive  
 258 and convective shell (Ruzmaikin 1991, Hubbard et al. 1995, Podolak et al., 1995, Stanley et al. 2004, Stanley et al.  
 259 2006, Soderblum and Stanley, 2020). The magnetic field model developed from the *Voyager 2* data (Connerney et  
 260 al. 1991) is described by the negative gradient of the scalar potential,  $\mathbf{B}_N = -\nabla V$ . The spherical harmonic expansion  
 261 of the scalar potential is expressed as

$$263 V = R_N \sum_{n=1}^N \left(\frac{R_N}{r}\right)^{n+1} \sum_{m=0}^n \{P_n^m(\cos\theta)[g_n^m \cos(m\phi) + h_n^m \sin(m\phi)]\}, \quad (1)$$

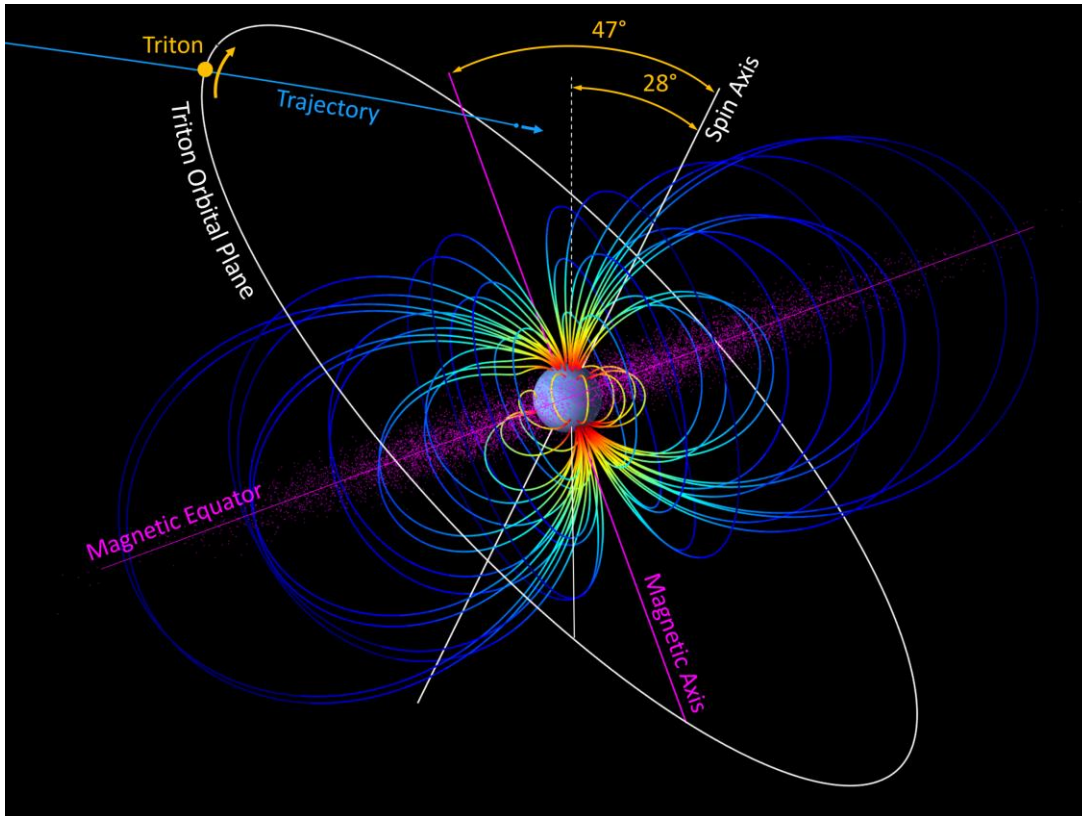
264 where  $R_N$  is equatorial radius of Neptune;  $r$  is the radial distance to the center of the planet;  $\theta$  is the colatitude;  $\phi$  is  
 265 the longitude;  $P_n^m(\cos\theta)$  are the Schmidt-normalized Legendre functions of degree  $n$  and order; and  $g_n^m$ ,  $h_n^m$  are  
 266 the internal Schmidt coefficients.

267 Figure 3 illustrates the magnetic field lines and magnitude associated with this model, including the large tilt ( $47^\circ$ )  
 268 of Neptune's magnetic axis with respect to its spin axis (which is titled  $28^\circ$  respect to the normal of the orbital  
 269 plane), and the highly inclined tilt of Triton's orbit. Evaluating the field model at the position of Triton reveals that  
 270 the moon experiences variations in the field at Triton's orbital period ( $T_{orbit} = 141$  hours) due to its orbital  
 271 inclination and also experiences variations in the magnetic field due to Neptune's rotation. As Neptune rotates every  
 272  $T_{spin} = 16.1$  hours, the apparent rotation period of the planet observed from Triton (i.e., the synodic period) is  
 273 defined by  $T_{synodic} = 1/(1/T_{spin} + 1/T_{orbit})$ , roughly every 14.5 hours. Note that the synodic period is shorter  
 274 than Neptune's rotation period due to Triton's retrograde orbit.

275 The left panel of Figure 4 illustrates the magnetic field time series of Neptune evaluated at the position of Triton and  
 276 the top right panel of the figure represents the associated frequency spectrum. In the Triton reference frame, the z  
 277 axis is aligned with Triton's spin axis, the x axis is in the direction of Neptune, and the y axis completes the right-  
 278 handed orthogonal system, roughly in the direction of the moon's orbital motion. Aside from the presence of the two  
 279 dominant variations of the magnetic field that occur at the prime frequencies, the 14-hour synodic period and the  
 280 141-hour orbital period, there are also variations that occur at the beats and harmonics of these two fundamental  
 281 periods. This AC portion of the magnetic field time series of Neptune  $\mathbf{B}_N$  at Triton can be modeled by a linear  
 282 superposition of sinusoids,

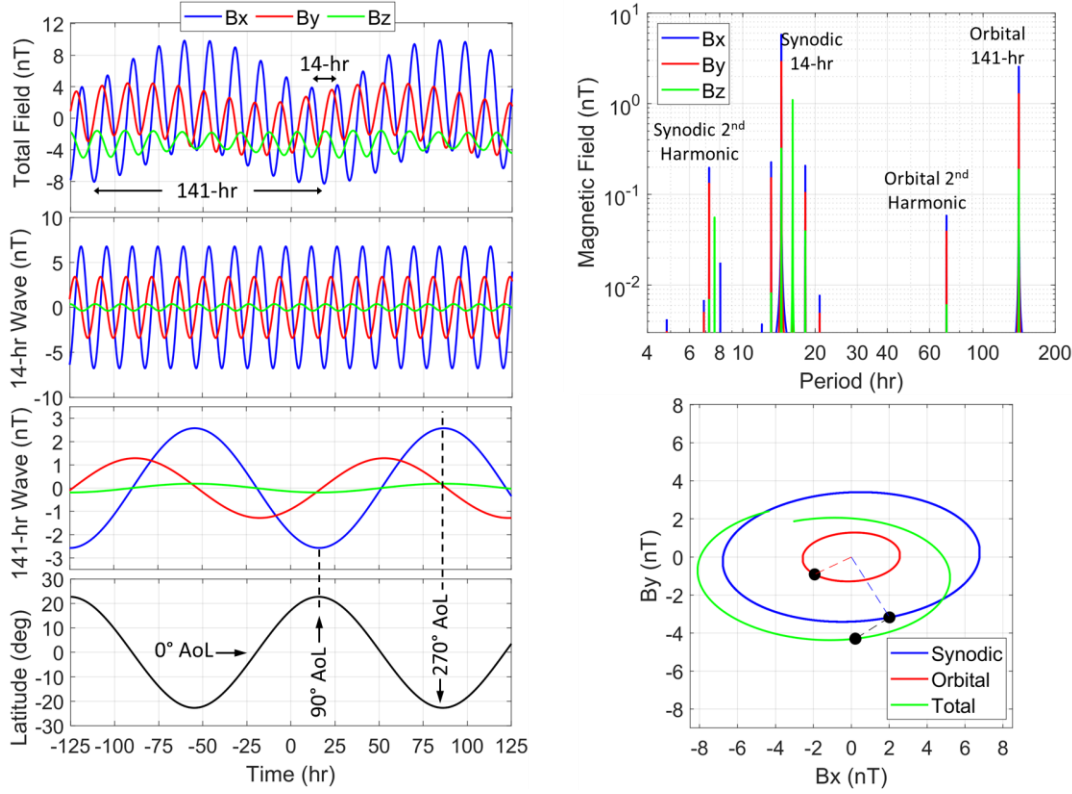
$$287 \mathbf{B}_N(t) = \sum_k \mathbf{B}_{N,k}(t) = \sum_k \mathbf{B}_k e^{i(2\pi f_k t + \theta_k)}, \quad (2)$$

288 where  $\mathbf{B}_{N,k}(t)$  is the  $k$ th discrete magnetic wave of Neptune at frequency  $f_k$ ,  $\mathbf{B}_k = [B_{x,k} \ B_{y,k} \ B_{z,k}]$  are their  
 289 amplitudes and  $\theta_k = [\theta_{x,k} \ \theta_{y,k} \ \theta_{z,k}]$  are their phases (referenced with respect to the J2000 epoch in this work). The  
 290 individual waves with the 15 largest amplitudes are used for analysis as illustrated in the top right of Figure 4 (see  
 291 Appendix for a complete table of magnitudes and phases for each of these waves, solved using a least-squares  
 292 inversion approach on the magnetic-field time series). Note that the strength of the orbital wave ( $B_x = 2.6$  nT) is the  
 293 same order of magnitude of the synodic wave ( $B_x = 6.8$  nT) which can cause the total magnetic moments to add  
 294 constructively or destructively in a significant fashion (see Section 6.2). This coincidence is not encountered at any  
 295 other potential ocean world in the solar system, making Triton an ideal body for multi-frequency magnetic induction  
 296 investigation.



298  
299  
300  
301  
302  
303  
304

**Figure 3:** Geometrical representation of the Neptune system, illustrating the tilt of Neptune's spin axis, the tilt of the Neptune's magnetic axis with respect to its spin axis, the orbit of Triton, the magnetic equator populated with corotating plasma particles, and the baseline trajectory of the spacecraft used in this work.



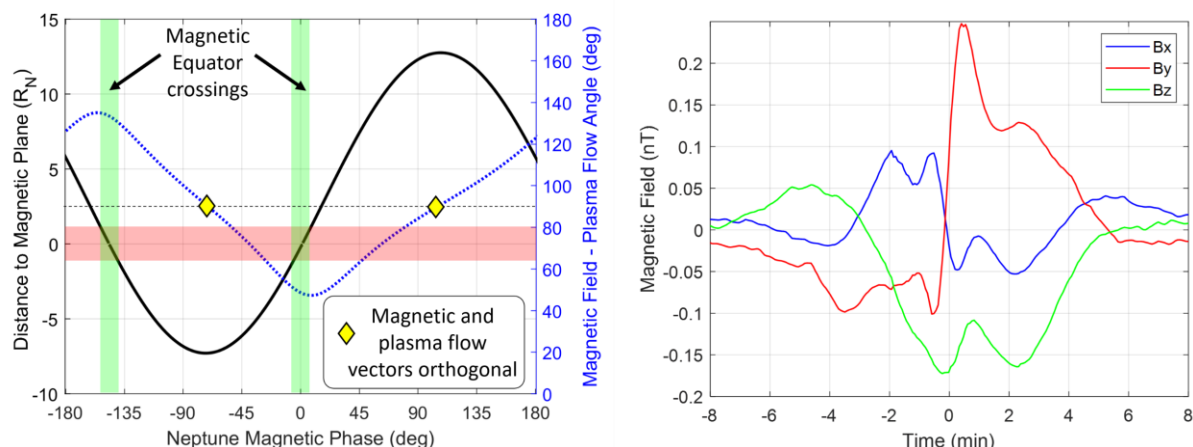
305  
306  
307 **Figure 4:** The combination of Neptune's tilted spin axis and Triton's inclined orbit causes the magnetic field to vary  
308 at multiple frequencies in Triton's fixed frame, dominated by Neptune's 14-hr synodic period and Triton's 141-hr  
309 orbital period. This is important in the context that the interaction path length is greater for longer period magnetic  
310 waves, thus the 141-hr period wave penetrates conductive layers, such as Triton's ionosphere, more readily. (left  
311 panel) From top-to-bottom, the total magnetic field time series evaluated at the orbit of Triton, the 14-hour synodic  
312 magnetic field time-series components, the 141-hour magnetic field time-series components, and Triton's latitudinal  
313 position in Neptune's geographic frame. (top right) Magnetic field spectrum of the time series illustrated in the top  
314 left plot. (bottom right) Hodograph comparing the  $B_x$  and  $B_y$  components (in IAU Triton frame) of Neptune's  
315 synodic, orbital, and total magnetic waves observed in the Triton reference frame. The total wave in this image only  
316 spans about +/- 7 hours with respect to closest approach, where the time of closest approach is indicated by the  
317 black dots along each curve.  
318

319 Also plotted in the left panel of Figure 4 along with the total magnetic field time-series are depictions of the time  
320 series broken down into the individual synodic and orbital periods. The phase of the synodic field illustrated is based  
321 on the Connerney et al., (1991) magnetic field model of Neptune (referenced in this work as 0° magnetic phase) but  
322 will be unknown until future spacecraft arrival. The magnetic phase is unknown because the rotation of Neptune's  
323 core is not visible from Earth and no spacecraft have visited the Neptune system since Voyager 2 in 1989.  
324 Furthermore, remote observations of aurora at Neptune, which could help to identify and constrain the location of  
325 the magnetic poles, remains elusive (Lamy et al., 2020). Note that the orbital or 141-hour magnetic wave field  
326 strength is maximized when Triton is at the highest Neptune latitude (+/- 23°), corresponding to an orbital argument  
327 of latitude (AoL) of 90° and 270°. Because Triton's orbit is almost perfectly circular, variations in the magnetic field  
328 are not attributable to change in distance with respect to Neptune, but rather are due to changes in position with  
329 respect to Neptune's magnetic latitude because the field is two times stronger at the poles of the dipole than at the  
330 magnetic equator.  
331

332 In addition to Triton's ionosphere induction response, Triton's magnetic environment is also affected by the moon's  
333 interaction with the magnetospheric plasma. The density of the ambient plasma fluctuates by nearly an order of  
334 magnitude as Neptune's magnetic equator and plasma sheet sweep over Triton. As a result, the interaction between  
335 the magnetospheric plasma, Triton's atmosphere/ionosphere, and induced field is time-variable. As shown in Figure

336 5 (left), Triton spends the majority of its orbit far from Neptune's magnetic equator, in regions where the magnetic  
 337 field perturbations associated with Triton's plasma interaction are negligible compared to the strength of the induced  
 338 field. During the short intervals when Triton traverses Neptune's magnetic equator (coincidentally corresponding to  
 339 a time associated with the baseline trajectory used in this work), results of hybrid modeling (Liuzzo et al., 2021)  
 340 indicate that the magnitude of plasma interaction fields will be minimal with perturbations below 10% of the  
 341 background field (see Figure 5 right) even when conservatively assuming a plasma density an order of magnitude  
 342 higher than measured by Voyager 2.  
 343

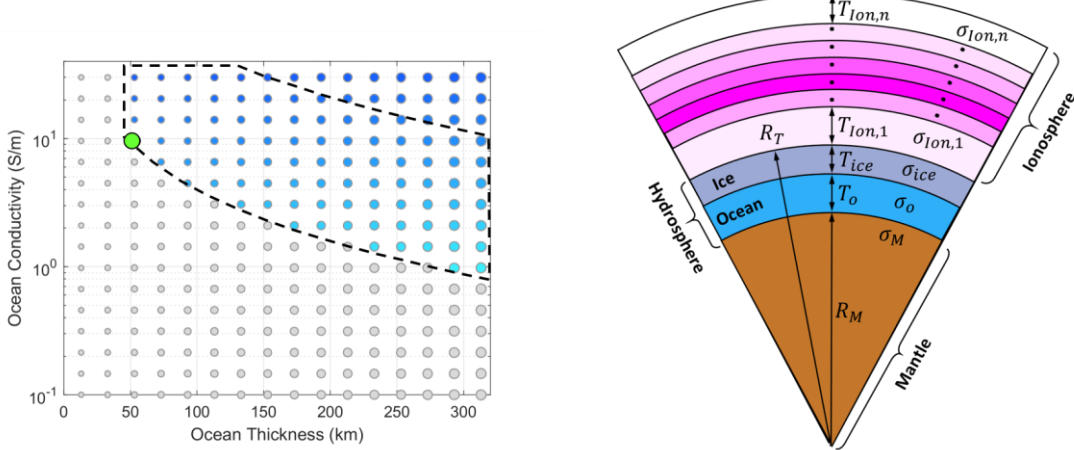
344 Moreover, the flow direction of  $47^\circ$  with respect to the background field is more favorable than the  $90^\circ$  cases that  
 345 fortuitously occur when the center of the plasma sheet is more than  $3 R_N$  distant. The  $47^\circ$  or  $133^\circ$  flow direction  
 346 reduces the perturbing effects that plasma interaction fields could have on the induced magnetic field originating  
 347 from a subsurface ocean. Moons in the Jovian system commonly experience strong plasma interaction effects due to  
 348 the high density of particles in the current sheet and orthogonal orientation of Jupiter's field with respect to this  
 349 current system (e.g., Liuzzo et al., 2016; 2017; 2018). Triton not only experiences much weaker plasma density (and  
 350 associated currents), but its highly inclined orbit and Neptune's magnetic rotational geometry further reduce the  
 351 perturbing effects of the plasma interaction to the point where it can be simply treated as a systematic noise source  
 352 for ocean detection purposes.  
 353



354  
 355  
 356 **Figure 5:** Interference from the plasma interaction is not anticipated to be significant for ocean detection at Triton.  
 357 (left) Triton's distance from Neptune's magnetic equator (black solid line) and the magnetic field – plasma flow  
 358 angle (dotted blue line) are shown as a function of Neptune magnetic phase at the 14-hour synodic period. The red  
 359 bar indicates a region  $\pm R_N$  about the magnetic equator, representing a region where plasma currents are  
 360 anticipated to be at their strongest. (right) Hybrid-modeling indicates that plasma interaction fields (isolated from  
 361 the induced dipole response of Triton) along the baseline trajectory resulting from the plasma currents in Neptune's  
 362 magnetosphere are of minimal magnitude (corresponding to  $0^\circ$  magnetic phase and  $50^\circ$  argument of latitude).  
 363

### 364 3.2 Ocean and Ionosphere Parameter Space Definition

365 Inclusion of a wide range of ocean, ionosphere and ice-shell characteristics that could realistically be encountered at  
 366 Triton is a key element of the ocean detection forward modeling process, for both pathways in Figure 2. A set of  
 367 13,056 potential ocean and ionosphere models is defined, and for each model the induced dipolar field that could be  
 368 potentially detected is derived. Analysis of Voyager 2 data (Strobel et al. 1990) found a best-fit for the ionosphere  
 369 conductance in the range of 10,000–20,000 Siemens (S), but based on expected local magnetic field variations at  
 370 Triton, the range could likely extend to 4,000 to 36,000 S. Considering the potential for increased electron  
 371 concentrations and electron temperatures, and to add margin, 51 ionosphere conductance values ranging from 0 to  
 372 100,000 S were considered for this analysis.  
 373  
 374  
 375

376  
377

**Figure 6:** This analysis is informed by a deep exploration of a wide range of possible ocean and ionosphere parameters. (left) The 256 modeled oceans comprising the ocean parameter space used to forward model the various complex response functions associated with Triton; the size of the circles indicates relative ocean thickness (smaller circles represent thinner, and therefore deeper oceans for a given hydrosphere thickness), while the circles' color represents relative ocean conductivity. The models contained within the black dashed contour represent the members of the ocean parameter space that are geophysically most likely, with the green circle representing the case within this subset that is most difficult to detect (an ocean with a thickness of 50 km and 9 S/m conductivity). This ocean is referred to as the least-favorable likely ocean throughout this manuscript. Note that because salt mass is conserved in aqueous solution, thinner oceans are typically associated with higher conductivities, themselves a function of salt concentration. (right) Multi-shell model of Triton entails a non-conductive rocky mantle, a conductive ocean of thickness  $T_o$ , a non-conductive ice shell of thickness  $T_{ice}$ , and conductive ionosphere which can be modeled with an arbitrary number of conductive layers  $n$  of varying conductivity  $\sigma_{ion}$  and thickness  $T_{ion}$ .

For this analysis, 256 ocean models are defined which, combined with 51 ionosphere models, yield 13,056 model cases comprising the overall ocean/ionosphere parameter space. Key drivers of the ocean's induced response are its conductivity, thickness, and depth of the liquid layer below Triton's surface. The ocean models illustrated in Figure 6 (left) represent conductivity values ranging from 0.1 through 30 S/m (in log-linear increments) and thicknesses from 10 to 310 km in increments of 10 km.

Ocean conductivity is a function of the type and abundance of solutes that went into solution early in Triton's evolution, as well as the current solute concentration following top-down freezing of an icy shell. Conductivity – for which salinity is a proxy – is modeled based on a plausible range of initial ocean salinity values of 1 to 8 S/m (Castillo-Rogez et al. 2021). Increases in conductivity since initial ocean formation, including the possibility of saturation at ~24 S/m as a bounding case (e.g., Rebello et al., 2020), are modeled to account for an initially thicker ocean freezing out and becoming thinner over time. Additional parameters such as the water-to-rock ratio and temperature which play a secondary role in determining how much of the volatiles combine into minerals (e.g., CO<sub>2</sub> in carbonates) are also modeled (Castillo-Rogez et al. 2021).

The induced signal from a conductive ocean depends on the ocean's conductance, the product of its conductivity and thickness. A constant overall thickness of Triton's hydrosphere (its ice layer plus the liquid ocean; Figure 5 right) of 340 km is assumed for this analysis, taking Io's density (~3500 kg/m<sup>3</sup>) as a reference for Triton's core density, based on its likely dehydration following capture (Nimmo and Spencer, 2015). As a general rule, thinner oceans with lower conductivity are naturally the most difficult to detect because they induce a weaker signal at the point of measurement (the induced dipolar response decreases by 1/r<sup>3</sup>).

The ocean models shown in blue within the dashed black line in Figure 6 (left) represent ocean characteristics most likely to be found at Triton based on these assumed geophysical parameters. Among this subset of the 256 models, the least-favorable likely ocean, shown as a green circle in this and subsequent figures, represents the deepest of

416 these oceans with the lowest conductivity: a thickness of 50 km, located 290 km below Triton's surface, with  
 417 conductivity of 9 S/m (corresponding to an initial conductivity of 1 S/m prior to freezing).  
 418

419 To analytically explore the boundaries of ocean detectability with the PCA methodology in the presence of noise  
 420 sources and plasma interaction fields, a significantly larger ocean parameter space than is currently considered likely  
 421 from the geophysical perspective is defined. The ocean models shown in gray in Figure 6 (left) represent this  
 422 artificial extension of the ocean parameter space beyond the blue ocean models considered likely to occur. Of this  
 423 set of less likely cases, the least-favorable induced response would be from an extremely thin (10 km) ocean located  
 424 330 km below the surface of Triton, with a vanishingly small salinity of 0.1 S/m. Performance limits of the PCA  
 425 methodology for these cases are shown in subsequent figures in keeping with the blue/gray/green color scheme.  
 426

### 427 3.3 The Complex Response Function

428 The complex response function of a planetary body represents the amplitude and phase delay of the combined  
 429 induction response of a particular ionosphere and ocean profile. Magnetic induction measurements are sensitive to  
 430 ice-shell thickness and ocean depth as the strength of an induced dipolar field degrades per  $(R_T/r)^3$  where  $R_T$  is the  
 431 radius of Triton and  $r$  is the radius to the observation. Algorithms for computing the magnetic induction response  
 432 (see Equation 5) of concentrically stratified conductors, pioneered over 50 years ago (Eckhardt 1963) and recently  
 433 matured (Vance et al. 2021), determine the specific induction response for each model via a height-integrated  
 434 approach as shown in Figure 6 (right). Each shell has a unique conductivity and thickness. Although each specific  
 435 shell typically has uniform conductivity versus height or thickness, the ionosphere can be modeled with changing  
 436 conductivity versus height to better represent unique and relatively intense ionospheres.  
 437

438 The radius of each shell is measured from Triton's center, including the mantle, the liquid ocean, ice layers, and the  
 439 ionosphere up to an altitude of 800 km. The specific shell layer conductivity  $\sigma_\eta$  is also specified. The numerical  
 440 approach employed provides the ability to solve for the complex response function using a configurable number of  
 441 spherical shells of varying conductivity to represent any layer of the atmosphere/ionosphere or interior to simulate  
 442 conductivity gradients. This capability could be particularly beneficial for any trajectory that has the potential to  
 443 measure the conductivity structure of the ionosphere. The resulting solution defines the unique induction response  
 444 characteristics of a specific ionosphere and ocean model in the frequency domain:  $Q(f) = A(f)e^{-i\phi(f)}$ , where  $A$  is  
 445 amplitude and  $\phi$  is phase delay relative to Neptune's driving AC magnetic field at frequency  $f$ . For all ocean  
 446 worlds, phase delay – a characteristic of all electromagnetic signals that traverse through any ambient medium – is  
 447 especially important for ocean detection. The differential phase delay between ocean and no-ocean cases is a  
 448 distinctive factor in revealing the nature of the induced magnetic response. For example, while the difference in  
 449 phase delay between the least-favorable ocean and ionosphere-only models can range from 20° to 90° at the synodic  
 450 period (14-hr) when the ionosphere HIC is 10 kS or less, the difference in phase delay between these two model  
 451 classes at the orbital period (141-hr) can range from 20° to 50° for ionospheres with HIC of 100 kS or less. Thus, the  
 452 phase delay, especially at the orbital period, is a significant discriminating factor between the two model classes.  
 453 Additional plots are illustrated in Figure A1 of the appendix to better illustrate this points and mathematically  
 454 expressed by Eq. 6 in the next section.

455 Figure 7 illustrates the complex response function  $A_k e^{-i\phi_k}$  for Neptune's dominant magnetic waves (with  $k$   
 456 indicative of discrete frequency), for the synodic 14-hour period and the 141-hour Triton orbital period, in a  
 457 complex plane with real and imaginary axes for the large set of 13,056 ionosphere and ocean models defined in the  
 458 parameter space. By contrast with Figure 1, there is now a clear separation of the ionosphere-only and ionosphere-  
 459 plus-ocean model classes. The complex response function data for the 14-hour magnetic wave indicate that the  
 460 primary synodic magnetic wave has limited penetration for an ionosphere intensity greater than ~40,000 S due to the  
 461 low skin depth associated with a highly conducting ionosphere. This result indicates that detecting a potential  
 462 subsurface ocean in the presence of an intense ionosphere depends primarily on the 141-hour orbital magnetic wave.  
 463 The longer period of the 141-hour magnetic wave allows it to penetrate the full range of ionosphere intensities, with  
 464 clear separation between the least-favorable likely ocean (green circle) and the ionosphere-only models (magenta –  
 465 yellow). Primarily because of the dipolar field falloff, the response of deep, thin oceans with low salinity values of  
 466 0.1 S/m approaches that of the ionosphere-only models.  
 467

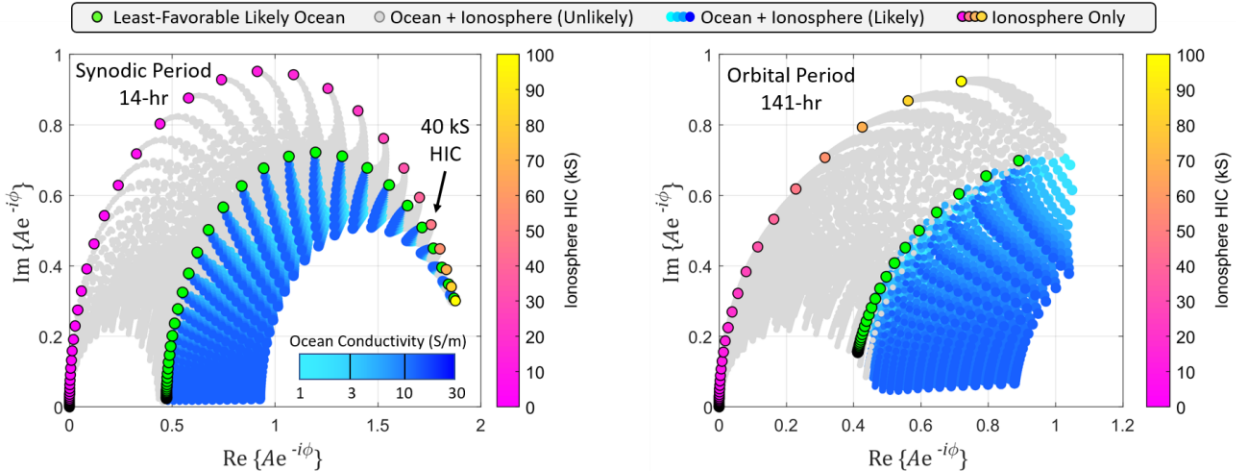


**Figure 7:** Triton's complex response functions evaluated at the frequencies corresponding to the synodic and orbital periods. (left) Complex plane representation of the complex response function for various combinations of ocean-plus-ionosphere models evaluated for the 14-hour synodic period of Neptune and the (right) 141-hour orbital period of Triton. The coloring of the ocean and ionosphere models corresponds to the scheme depicted in Figure 6. The green circles represent the least-favorable bounding case among the most likely ocean models, characterized by a thickness of 50 km and a conductivity of 9 S/m as depicted in Figure 6. Note that the ionosphere-only models and the ocean-plus-ionosphere models begin to overlay each other at the synodic period above ionosphere HIC of 40 kS, which stresses the usefulness of the orbital period where there is complete separation of model classes.

### 3.4 Total Induced Magnetic Moments

Ionosphere and ocean induced magnetic moments are responsible for the induced magnetic field that is measured by a passing spacecraft. This magnetic field along the trajectory in units of nT, is forward modeled using the real part of the dipole field equation defined by

$$\mathbf{B}_{Ind}(\mathbf{r}, t) = \text{Re} \left\{ \frac{\mu_0}{4\pi} \frac{3(\mathbf{r}(t) \cdot \mathbf{U}(t))\mathbf{r}(t) - r^2(t) \mathbf{U}(t)}{r^5(t)} \right\}. \quad (3)$$

Here,  $\mathbf{r}(t) = [x(t), y(t), z(t)]$  is the position of the spacecraft with respect to the center of the moon and  $\mathbf{U}(t)$  is the induced magnetic moment vector in units of A-m<sup>2</sup>, based on an induction model initially applied to the Jovian moons (Zimmer et al., 2000), defined by

$$\mathbf{U}(t) = \frac{4\pi}{\mu_0} \frac{R_T^3}{2} \mathbf{M}(t), \quad (4)$$

where  $\mu_0$  is the permeability of free space,  $R_T$  is the radius of Triton (1,353.4 km), and the time-varying portion of the moment vector  $\mathbf{M}(t) = [M_x(t), M_y(t), M_z(t)]$ , in units of nT, is defined by

$$\mathbf{M}(t) = - \sum_k A_k e^{-i\phi_k} \mathbf{B}_{N,k}(t). \quad (5)$$

The summation of terms in Equation 5 represents the total induced magnetic moment driven by Neptune's AC magnetic field  $\mathbf{B}_{N,k}(t)$  at the 15 discrete frequencies  $k$ , although the two primary (synodic and orbital) frequencies dominate. The complex response function  $A_k e^{-i\phi_k}$  represents a specific ionosphere-only or ionosphere-plus-ocean model where  $A_k$  is the relative amplitude and  $\phi_k$  is the phase delay or lag of the model's induction response at frequency  $k$  with respect to that which would be induced by a perfectly conducting sphere of radius  $R_T$ .

503 The real part of these magnetic moments can be represented by the summation of phase-delayed dominant magnetic  
 504 waves at various frequencies (see top right panel of Figure 4) multiplied by the amplitude of the associated complex  
 505 response function,

$$\begin{aligned} 507 \quad M_x(t) &= -\sum_k A_k B_{x,k} \cos(2\pi f_k t + \theta_{x,k} - \phi_k), \\ 508 \quad M_y(t) &= -\sum_k A_k B_{y,k} \cos(2\pi f_k t + \theta_{y,k} - \phi_k), \\ 509 \quad M_z(t) &= -\sum_k A_k B_{z,k} \cos(2\pi f_k t + \theta_{z,k} - \phi_k). \end{aligned} \quad (6)$$

510  
 511  
 512  
 513 The strength of the magnetic moments is therefore directly related to the amplitude of the complex response function  
 514  $A_k$  and the associated driving magnetic field strength of the specific  $k$  frequencies. However, the phase delay  $\phi_k$  is  
 515 also important in determining the strength of the magnetic moments associated with ionosphere-only and ocean-  
 516 plus-ionosphere models, and thus for discerning contributions of an ocean to the overall induction response.  
 517

### 518 3.5 Induced Dipole Magnetic Field Time-Series

519 To aid in the analysis, the magnetic induction fields (Eq. 3) are written conveniently in matrix notation. The forward  
 520 modeling of the 13,056 induced magnetic field time-series illustrated in Figure 1,  $B_{Ind,x}(t)$ ,  $B_{Ind,y}(t)$ , and  $B_{Ind,z}(t)$   
 521 can be expressed as a matrix multiplication of the dipolar matrix  $\mathbf{D}(t)$  and the total magnetic moment matrix  $\mathbf{M}(t)$ ,

$$523 \quad \mathbf{B}_{Ind}(t) = \mathbf{D}(t)\mathbf{M}(t), \quad (7)$$

524 where the 3-by-3 dipolar trajectory matrix is defined at time  $t$ ,

$$527 \quad \mathbf{D}(t) = \frac{R_T^3}{2} \frac{1}{r(t)^5} \begin{bmatrix} 3x(t)^2 - r(t)^2 & 3x(t)y(t) & 3x(t)z(t) \\ 3y(t)x(t) & 3y(t)^2 - r(t)^2 & 3y(t)z(t) \\ 3z(t)x(t) & 3z(t)y(t) & 3z(t)^2 - r(t)^2 \end{bmatrix}. \quad (8)$$

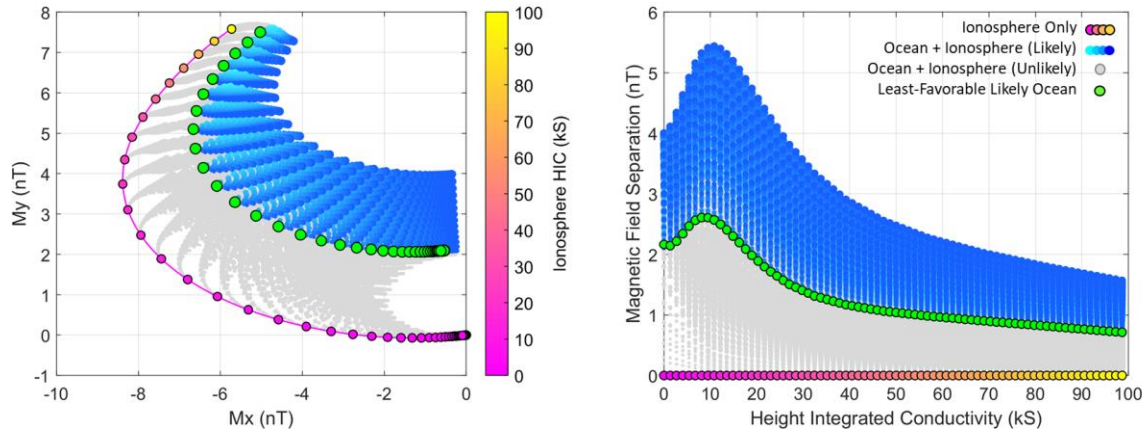
528 Because the velocity of the spacecraft is fast relative to changes in the magnetic waves experienced by Triton over  
 529 the 12-minute encounter, the magnetic moment vector is essentially stationary over the duration of the encounter and  
 530 can be approximated as a 3-element vector  $\mathbf{M} = [M_x(t_{ca}), M_y(t_{ca}), M_z(t_{ca})]$  where  $t_{ca}$  represents the spacecraft's  
 531 time at closest approach to Triton. Assuming the magnetometer acquires samples at a rate of  $F_s$  samples/second, the  
 532 discrete-time representation of the dipolar field time-series is formed by the substitution  $t = nT_s$ , where  $n$  is the  
 533 sample index and  $T_s = 1/F_s$  the sampling period in units of seconds. Equation 7 now becomes  
 534

$$536 \quad \begin{bmatrix} B_{Ind,x}(n) \\ B_{Ind,y}(n) \\ B_{Ind,z}(n) \end{bmatrix} = \begin{bmatrix} D_{11}(n) & D_{12}(n) & D_{13}(n) \\ D_{21}(n) & D_{22}(n) & D_{23}(n) \\ D_{31}(n) & D_{32}(n) & D_{33}(n) \end{bmatrix} \begin{bmatrix} M_x(n) \\ M_y(n) \\ M_z(n) \end{bmatrix}, \text{with } n = 1 \text{ to } N \quad (9)$$

537 A detailed ocean classification space, defined by the magnetic moments at closest approach  $M_x$ ,  $M_y$ , and  $M_z$ ,  
 538 represents the unique attributes of a range of potential sub-surface oceans and or ionospheric profiles. In the absence  
 539 of noise, each model in the classification space is unique and represents specific physical parameters (e.g. ice shell  
 540 thickness, ocean thickness and conductivity, and ionospheric conductance). The figure of merit for ocean detection  
 541 in this work is referred to as *magnetic separation* (MS), defined as the three-dimensional Euclidean distance  
 542 between the corresponding total induced magnetic moments of the ionosphere-only and ocean-plus-ionosphere  
 543 models, measured in units of nT. The  $M_z$  component of the total magnetic moments are small but do contribute to  
 544 the separation of model classes. The left panel of Figure 8 illustrates the magnetic moment classification space (only  
 545  $M_x$  and  $M_y$  shown) of the 13,056 forward models used in this study, computed using the 15 most dominant discrete  
 546 magnetic waves (per Equations 5 and 6). The magnetic separation of ocean-plus-ionosphere to ionosphere-only  
 547

models is illustrated in the right panel of Figure 8, plotted as a function of ionosphere HIC from 0 to 100,000 S. The ocean classification space presented in the figure represents the classification space of Path 1 of Figure 2 for an assumed 14-hour magnetic phase of zero (defined by Connerney et al. 1991). For an ionosphere HIC greater than ~50,000 S, magnetic separation drops below 1 nT which can be challenging for classification purposes in the presence of noise, especially when the full range of 14-hour magnetic phase is considered (Section 6.2). Thus, Section 4 focuses on increasing magnetic separation of the model classes using a concept called *scaled magnetic moments*, which is equivalent to the separation achieved by PCA (see Section 5).

555  
556  
557



558  
559  
560  
561  
562  
563  
564  
565

**Figure 8:** Ocean classification space defined by the induced magnetic moments. (left)  $M_x$  and  $M_y$  magnetic moment components for all forward modeled cases. (Note that there is also a third dimension representing the  $M_z$  component that is not shown due to its relatively small magnitude relative to the other two components.) (right) The magnetic separation between ionosphere-only and ocean-plus-ionosphere magnetic moments for all models as a function of ionosphere HIC.

## 4 Scaled Magnetic Moments (SMM)

As previously described, Path 2 of Figure 2 entails using PCA to directly process the induced magnetic field time-series  $B_{Ind,x}(n)$ ,  $B_{Ind,y}(n)$ , and  $B_{Ind,z}(n)$ . This approach leads to the concept of *scaled magnetic moments* discussed in this section.

571

### 4.1 Preservation of Signal Energy

572  
573  
574  
575  
576  
577  
578

Magnetic separation between distinct data classes can be increased when the signal energy, or the *spread* of the data (analogous to its standard deviation), associated with the induced dipolar field discrete time-series is retained in the analysis. The total discrete-time signal energy  $E_{signal}$  contained in the time series can be compactly written in terms of a scaled magnetic moment vector,

$$E_{signal} = \sum_{n=1}^N [B_{Ind,x}^2(n) + B_{Ind,y}^2(n) + B_{Ind,z}^2(n)] = M_1^2 + M_2^2 + M_3^2, \quad (10)$$

580  
581  
582  
583

where the scaled magnetic moment vector  $[M_1, M_2, M_3]$  is simply related to the time-varying portion of the induced magnetic moment vector  $[M_x, M_y, M_z]$  of the forward model through a 3-by-3 scaling matrix  $S_{SMM}$ ,

584 
$$\begin{bmatrix} M_1 \\ M_2 \\ M_3 \end{bmatrix} = \begin{bmatrix} S_{11} & S_{12} & S_{13} \\ S_{21} & S_{22} & S_{23} \\ S_{31} & S_{32} & S_{33} \end{bmatrix} \begin{bmatrix} M_x \\ M_y \\ M_z \end{bmatrix}. \quad (11)$$

585  
 586 The closed form notation of Equation 11 indicates the possibility of viewing the induced dipolar fields in a reduced  
 587 dimensionality, suggesting that PCA provides a viable methodology to perform this task. As will be shown in  
 588 Section 5, the principal components produced by PCA are directly related to the scaled magnetic moment detailed  
 589 here and effectively result in identical magnetic separation of ionosphere-only and ocean-plus-ionosphere model  
 590 classes.

591 By multiplying out Equation 11 and inserting into Equation 10, the coefficients of the 9-element scaling matrix  
 592  $\mathbf{S}_{SMM}$  can be solved for analytically. Because there are 9 unknowns and 6 equations, the resulting system is  
 593 underdetermined. However, the scaling matrix can be readily constrained to be symmetrical about the diagonal (e.g.,  
 594 off-diagonal terms are mirrored) or more conveniently, 3 of the 9 elements simply set to zero. The coefficients are  
 595 defined by,

596  $S_{11} = \sqrt{C_{xx}} \quad (12a)$

597  $S_{12} = C_{xy}/\sqrt{C_{xx}} \quad (12b)$

598  $S_{13} = C_{xz}/\sqrt{C_{xx}} \quad (12c)$

599  $S_{22} = (C_{yy} - S_{12}^2)^{1/2} \quad (12d)$

600  $S_{23} = (C_{yz} - S_{12}S_{13}/C_{xx})/S_{22} \quad (12e)$

601  $S_{33} = (C_{zz} - S_{13}^2 - S_{23}^2)^{1/2} \quad (12f)$

602  $S_{21} = S_{31} = S_{32} = 0, \quad (12g)$

603 where the constants  $C_{xx}$ ,  $C_{yy}$ ,  $C_{zz}$ ,  $C_{xy}$ ,  $C_{xz}$ , and  $C_{yz}$  are defined by:

604  $C_{xx} = \sum_{n=1}^N [D_{11}(n)^2 + D_{21}(n)^2 + D_{31}(n)^2] \quad (13a)$

605  $C_{yy} = \sum_{n=1}^N [D_{12}(n)^2 + D_{22}(n)^2 + D_{32}(n)^2] \quad (13b)$

606  $C_{zz} = \sum_{n=1}^N [D_{13}(n)^2 + D_{23}(n)^2 + D_{33}(n)^2] \quad (13c)$

607  $C_{xy} = \sum_{n=1}^N [D_{11}(n)D_{12}(n) + D_{21}(n)D_{22}(n) + D_{31}(n)D_{32}(n)] \quad (13d)$

608  $C_{xz} = \sum_{n=1}^N [D_{11}(n)D_{13}(n) + D_{21}(n)D_{23}(n) + D_{31}(n)D_{33}(n)] \quad (13e)$

609  $C_{yz} = \sum_{n=1}^N [D_{12}(n)D_{13}(n) + D_{22}(n)D_{23}(n) + D_{32}(n)D_{33}(n)]. \quad (13f)$

## 610 4.2 Magnetic Separation of Scaled Magnetic Moments

611 A key figure of merit of the proposed ocean detection methodology involves the magnetic separation (MS) of two  
 612 model classes in a multi-dimensional space [ $MS_1$ ,  $MS_2$ ,  $MS_3$ ]. This MS can be directly calculated with the use of the  
 613 scaling matrix  $\mathbf{S}_{SMM}$  (with coefficients given by Eq. 12) and the MS between ocean and no-ocean magnetic  
 614 moments [ $MS_x$ ,  $MS_y$ ,  $MS_z$ ], represented in Figure 8,

615

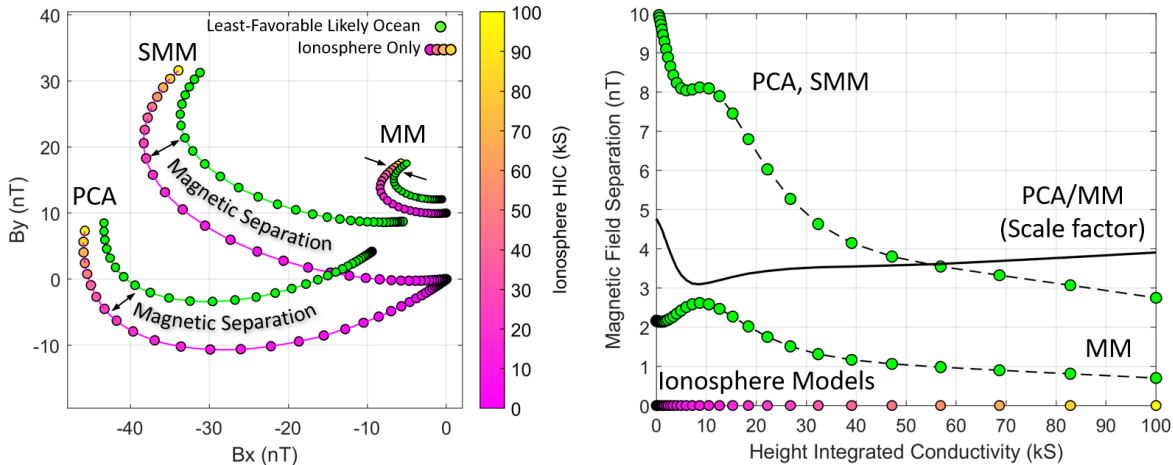
621

$$\begin{bmatrix} MS_1 \\ MS_2 \\ MS_3 \end{bmatrix} = \begin{bmatrix} S_{11} & S_{12} & S_{13} \\ 0 & S_{22} & S_{23} \\ 0 & 0 & S_{33} \end{bmatrix} \begin{bmatrix} M_{x,ocean} - M_{x,ion} \\ M_{y,ocean} - M_{y,ion} \\ M_{z,ocean} - M_{z,ion} \end{bmatrix} = \begin{bmatrix} S_{11} & S_{12} & S_{13} \\ 0 & S_{22} & S_{23} \\ 0 & 0 & S_{33} \end{bmatrix} \begin{bmatrix} MS_x \\ MS_y \\ MS_z \end{bmatrix}, \quad (14)$$

622

623 where  $[M_{x,ocean}, M_{y,ocean}, M_{z,ocean}]$  corresponds to the magnetic moment associated with a representative ocean-  
 624 plus-ionosphere model and  $[M_{x,ion}, M_{y,ion}, M_{z,ion}]$  corresponds to the magnetic moment of the associated  
 625 ionosphere model it was convolved with. Figure 9 (left) illustrates the scaled total magnetic moments - for brevity  
 626 abbreviated SMM - compared to the total magnetic moments (MM) that would be obtained in Path 1 of Figure 2.  
 627 The ionosphere-only models are compared to those for the ionospheres convolved with the least-favorable likely  
 628 ocean cases (green circles) across the ionosphere intensity range of 0 to 100,000 S. Figure 9 (right) compares  
 629 magnetic separation across this intensity range, assuming a magnetometer sampling rate of one sample per second.  
 630 Note that the scaled magnetic moments exhibit significantly increased separation compared to the original magnetic  
 631 moments obtained through the inversion methodology of Path 1. As a foreshadow to the results of PCA discussed in  
 632 the next section, the principal components of the dipolar field time-series are also shown in the figure and, as  
 633 illustrated, result in *identical* magnetic separation to that of the scaled magnetic moments. The PCA results exhibit a  
 634 rotation as compared with the SMM data derived in Equation 14, but this is simply a characteristic of the tool and is  
 635 not relevant to the separation between model classes and hence ocean detection. The rotation occurs because PCA  
 636 maximizes data variability for its primary principal component axis (PC1), followed by PC2 and then PC3.  
 637

638



639

640 **Figure 9:** Data dimensionality reduction of the induced magnetic field time-series results in increased magnetic  
 641 separation compared to that exhibited by the induced magnetic moments. (left) Comparison of the magnetic  
 642 separation for the magnetic moments (MM, offset in +y by 10 nT for visual clarity), scaled magnetic moments  
 643 (SMM) acquired by the analytical approach, and PCA method for all of the ionosphere-only models (magenta) and  
 644 ionosphere-plus-ocean models relative to the least-favorable bounding ocean case (green), with thickness of 50 km  
 645 and 9 S/m conductivity. (right) Plot of magnetic separation (distance measured in a 3-dimensional space) achieved  
 646 by each of the three methods. Note that the analytical approach exactly replicates the magnetic separation achieved  
 647 by PCA. Also note the increase in separation achieved by PCA, represented in terms of the scale factor by the black  
 648 solid line.

649

#### 650 4.3 Linear Transform of the Induced Dipole Field Time-Series to M1, M2 & M3

651

652 The dipolar induction fields noted by Equation 9 can be expressed conveniently in matrix form by  $\mathbf{B} = \mathbf{DM}$  for all  
 653 time  $t$ , written in expanded form by

654

$$\begin{matrix}
 B_{Ind,x}(1) \\
 \vdots \\
 B_{Ind,x}(N) \\
 B_{Ind,y}(1) \\
 \vdots \\
 B_{Ind,y}(N) \\
 B_{Ind,z}(1) \\
 \vdots \\
 B_{Ind,z}(N)
 \end{matrix}
 = \begin{bmatrix}
 D_{11}(1) & D_{12}(1) & D_{13}(1) \\
 \vdots & \vdots & \vdots \\
 D_{11}(N) & D_{12}(N) & D_{13}(N) \\
 D_{21}(1) & D_{22}(1) & D_{23}(1) \\
 \vdots & \vdots & \vdots \\
 D_{21}(N) & D_{22}(N) & D_{23}(N) \\
 D_{31}(1) & D_{32}(1) & D_{33}(1) \\
 \vdots & \vdots & \vdots \\
 D_{31}(N) & D_{32}(N) & D_{33}(N)
 \end{bmatrix} \begin{bmatrix} M_x \\ M_y \\ M_z \end{bmatrix}. \quad (15)$$

655

Matrix  $\mathbf{B}$  is a  $3N$ -by-1 vector representing the component interleaved induced magnetic field time-series  $\mathbf{B}_{Ind}(n)$  and  $\mathbf{D}$  is a  $3N$ -by-3 matrix which represents the dipolar matrix terms of Equation 9.  $\mathbf{M} = [M_x, M_y, M_z]$  is the associated time-varying portion of the magnetic moment vector, assumed to be static at closest approach, expressed as a 3-by-1 vector. This vector can be solved via least squares inversion, effectively by taking the product of the pseudo-inverse of the matrix  $\mathbf{D}$  and the magnetic field time-series  $\mathbf{B}$ ,

662

$$\mathbf{M} = [(\mathbf{D}'\mathbf{D})^{-1}\mathbf{D}']\mathbf{B}. \quad (16)$$

664

Using this estimate of the magnetic moment, the scaled magnetic moment vectors  $[M_1, M_2, M_3]$  are computed by multiplying through with the derived scaling matrix  $\mathbf{S}_{SMM}$ , with coefficients defined by Equations 12,

667

$$\begin{bmatrix} M_1 \\ M_2 \\ M_3 \end{bmatrix} = \mathbf{S}_{SMM}[(\mathbf{D}'\mathbf{D})^{-1}\mathbf{D}']\mathbf{B} = \mathbf{V}_{SMM}\mathbf{B} = \begin{bmatrix} v_1(1) & \dots & v_1(3N) \\ v_2(1) & \dots & v_2(3N) \\ v_3(1) & \dots & v_3(3N) \end{bmatrix} \begin{bmatrix} B_{Ind,x}(1) \\ \vdots \\ B_{Ind,x}(N) \\ B_{Ind,y}(1) \\ \vdots \\ B_{Ind,y}(N) \\ B_{Ind,z}(1) \\ \vdots \\ B_{Ind,z}(N) \end{bmatrix}, \quad (17)$$

669

yielding an equivalent 3-by-3N projection matrix (similar to the PCA eigenvectors discussed in subsequent sections) defined by  $\mathbf{V}_{SMM} = \mathbf{S}_{SMM}(\mathbf{D}'\mathbf{D})^{-1}\mathbf{D}'$ . Equation 17 can now be used to project a forward-modeled magnetic field time-series (or a noisy measurement) into the scaled magnetic moment classification space, similar to that illustrated in Path 2 of Figure 2.

## 674 5 Principal Component Analysis (PCA)

### 675 5.1 PCA Design Matrix

676 PCA is a powerful data dimensionality reduction technique that has been extensively used for feature extraction and  
 677 classification in a wide variety of scientific and engineering disciplines (Jolliffe et al. 2016, Hannachi et al. 2007,  
 678 Alken et al. 2017), but has not been previously applied to magnetic induction datasets for planetary ocean detection  
 679 or characterization. The power of PCA lies in its ability to identify patterns and correlation between features in  
 680 large, complex datasets such as the forward modeled magnetic field time series data. The method aims to find the  
 681 axes of maximum variance in high-dimensional data (the number of samples  $N$  over time being the dimension in  
 682 this case) and projects it onto a new subspace of *principal components* (PCs) with fewer dimensions using a linear  
 683 transformation. For ocean detection purposes, PCA provides a *classification space* that defines two distinct clusters  
 684 of ocean-plus-ionosphere and ionosphere-only models, which can be distinguished by a 3-dimensional boundary,  
 685 based on principal components of the induced dipolar field time-series. PCA projects the 13,056 forward modeled  
 686 magnetic induction fields into the classification space defined by  $PC_1$ ,  $PC_2$ , and  $PC_3$  as illustrated in Path 2 of Figure  
 687 2. This three-dimensional classification space yields identical magnetic field separation between the two model  
 688 classes as the scaled magnetic moments ( $M_1, M_2, M_3$ ) presented in the previous section.  
 689

690 PCA provides the additional benefit of being able to process the measurements made from the magnetometer  
 691 directly after subtraction of the Neptune background field. Additional flexibility is gained in that not all  
 692 magnetometer channels are required for ocean detection purposes (see Section 7.1), additional ocean discrimination  
 693 occurs, and improved characterization is achieved for multiple flybys (Sections 6.3 and 9).  
 694

695 The first step in the PCA ocean detection algorithm is concatenating the three channels of the induced dipolar  
 696 magnetic field time-series (each  $N$  samples long) for each of the  $P$  forward models (13,056 in this analysis) to form  
 697 a matrix as input to PCA. The  $3N$  samples for each of the  $P$  forward models are stored vertically in a matrix  $\mathbf{Y}$  with  
 698 dimension  $3N$ -by- $P$  as illustrated in Equation 18a. These data are centered by subtracting out the mean across each  
 699 row time index to create a design matrix  $\mathbf{X}$  (Equation 18b). Figure 10 (top) illustrates the centered three channels of  
 700 the forward modeled induced dipolar magnetic field time-series (each  $N$  samples long and with the background field  
 701 removed) for all ionosphere-only (magenta) and ocean-plus-ionosphere (shades of blue) models, in addition to a  
 702 representative noisy measurement (orange). The matrix denoted by Equation 18b is directly input into the PCA  
 703 ocean detection routine.  
 704

$$705 \quad \mathbf{Y} = \begin{bmatrix} B_{Ind,x,1}(1) & \cdots & B_{Ind,x,P}(1) \\ \vdots & & \vdots \\ B_{Ind,x,1}(N) & \cdots & B_{Ind,x,P}(N) \\ B_{Ind,y,1}(1) & \cdots & B_{Ind,y,P}(1) \\ \vdots & & \vdots \\ B_{Ind,y,1}(N) & \cdots & B_{Ind,y,P}(N) \\ B_{Ind,z,1}(1) & \cdots & B_{Ind,z,P}(1) \\ \vdots & & \vdots \\ B_{Ind,z,1}(N) & \cdots & B_{Ind,z,P}(N) \end{bmatrix} \quad (18a) \quad \mathbf{X} = \begin{bmatrix} B_{Ind-C,x,1}(1) & \cdots & B_{Ind-C,x,P}(1) \\ \vdots & & \vdots \\ B_{Ind-C,x,1}(N) & \cdots & B_{Ind-C,x,P}(N) \\ B_{Ind-C,y,1}(1) & \cdots & B_{Ind-C,y,P}(1) \\ \vdots & & \vdots \\ B_{Ind-C,y,1}(N) & \cdots & B_{Ind-C,y,P}(N) \\ B_{Ind-C,z,1}(1) & \cdots & B_{Ind-C,z,P}(1) \\ \vdots & & \vdots \\ B_{Ind-C,z,1}(N) & \cdots & B_{Ind-C,z,P}(N) \end{bmatrix} \quad (18b)$$

706  
 707  
 708 

## 5.2 PCA Covariance Matrix and Eigenvectors

  
 709 The next step in the method is computing the covariance matrix, defined by  $\mathbf{XX}'$ , which has dimension  $3N$ -by- $3N$ .  
 710 PCA effectively performs an eigenvalue decomposition of the covariance matrix which yields a set of eigenvectors  
 711  $\mathbf{V}_{PCA}$ , each of length  $3N$ , defined by  
 712  
 713

$$714 \quad \mathbf{V}_{PCA} = \begin{bmatrix} v_1(1) & \cdots & v_{3N}(1) \\ \vdots & & \vdots \\ v_1(3N) & \cdots & v_{3N}(3N) \end{bmatrix}. \quad (19)$$

715 The PCA eigenvectors represent the axes of greatest variability, where the amount of variability is defined by its  
 716 associated eigenvalue. The  $PC_1$  eigenvector represents the basis transformation associated with the axis of greatest  
 717 variance in the data and is used to project the data into the new lower-dimension classification space. Thus, the  
 718 signal variation associated with  $PC_1$  will always be the highest and contain the most information (e.g. signal  
 719 variance). As the three eigenvectors associated with the largest three eigenvalues represent more than 99.99% of the  
 720 variation of the data for a single flyby, retention of only those three is sufficient to accurately project the high  
 721 dimensionality data contained in the design matrix  $\mathbf{X}$  onto the 3-dimension PC classification space. These three  
 722 eigenvectors,  $v_1$ ,  $v_2$ , and  $v_3$ , are plotted as a function of sample number in the bottom panel of Figure 10. Note the  
 723 similarity of the line shape of the eigenvectors with the induced magnetic field responses illustrated in the upper  
 724 panel. It is the dipolar matrix that results in the unique shape of the magnetic induction fields in the top panel of  
 725 Figure 10 as the magnetic moments are near constant as a result of the relatively short encounter time (12-minutes).  
 726 The dipolar matrix is also common to all of the PCA input data. As such, the shape of the dipolar matrix coefficients  
 727 as a function of time govern the shape of the eigenvectors extracted from the covariance matrix.  
 728

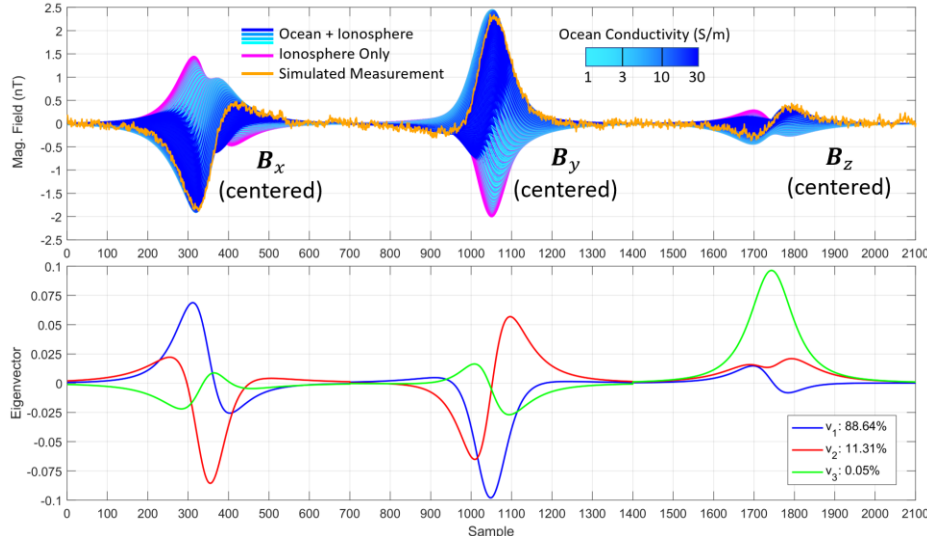


**Figure 10:** The eigenvector decomposition results in a set of eigenvectors that resemble the structure of the induced magnetic field time-series. (top) Columns of the design matrix  $\mathbf{X}$ , formed from the centered magnetic induction fields of the forward modeled ocean-plus-ionosphere (blue) and ionosphere-only (magenta) models, plotted as a function of sample number. Also plotted in the panel is a representative noisy measurement of the induced magnetic field components (orange), concatenated and centered. (bottom) The top three eigenvectors extracted from the covariance matrix. Here,  $v_1$  explains 88.64% of the data variance,  $v_2$  explains 11.31% of the data variance, and  $v_3$  explains 0.05% of the data variance.

### 5.3 Linear Transform of Induced Dipole Field Time-Series to PC1, PC2 & PC3

Without any loss of information, the principal components associated with each of the  $P$  models are computed by the projection operation,  $\mathbf{PC} = \mathbf{V}'_{PCA} \mathbf{X}$ , and the top three PCs ( $PC_1, PC_2, PC_3$ ) are retained for each model as they contain all of the information in the time-series. The PCs associated with the  $p$ th model are computed by

$$\mathbf{PC}_p = \mathbf{V}'_{PCA} \mathbf{X}_p = \begin{bmatrix} PC_{1,p} \\ PC_{2,p} \\ PC_{3,p} \end{bmatrix} = \begin{bmatrix} v_1(1) & \dots & v_1(3N) \\ v_2(1) & \dots & v_2(3N) \\ v_3(1) & \dots & v_3(3N) \end{bmatrix} \begin{bmatrix} B_{Ind-C,1,p} \\ \vdots \\ B_{Ind-C,3N,p} \end{bmatrix} \quad (20)$$

where  $\mathbf{X}_p$  represents the  $p$ th column in  $\mathbf{X}$ . When an actual (noisy) observation is made from a spacecraft in the vicinity of the potential ocean world, the planetary background field is subtracted using a polynomial fitting routine as a first processing step, the three magnetometer channels are concatenated and centered to form the vector  $\mathbf{X}_M$  ( $M$  for measurement), and then projected into the reduced dimension PC classification space using the eigenvectors  $\mathbf{V}_{PCA}$  associated with the noise-free forward modeled data,  $\mathbf{PC}_M = \mathbf{V}'_{PCA} \mathbf{X}_M$ . Figure 11 conceptualizes the projection of the representative noisy simulated observation, colored in orange, into the classification space defined by all the other  $P$  forward models.

It should be pointed out that not only does this methodology serve as a binary classifier of ocean versus no-ocean outcomes, but it also serves as a tool for characterization of ocean properties. The absolute position in PC space provides a direct correspondence to ocean and ionosphere parameters because each forward modeled ocean represents a unique interior configuration. Thus, depending on where the projected measurement lands in the classification space, inferences can be made regarding key ocean properties such as ocean thickness and conductivity. The amount of noise on the measurements will dictate the constraints that can be placed on these key interior parameters and will be discussed in Section 7.2.

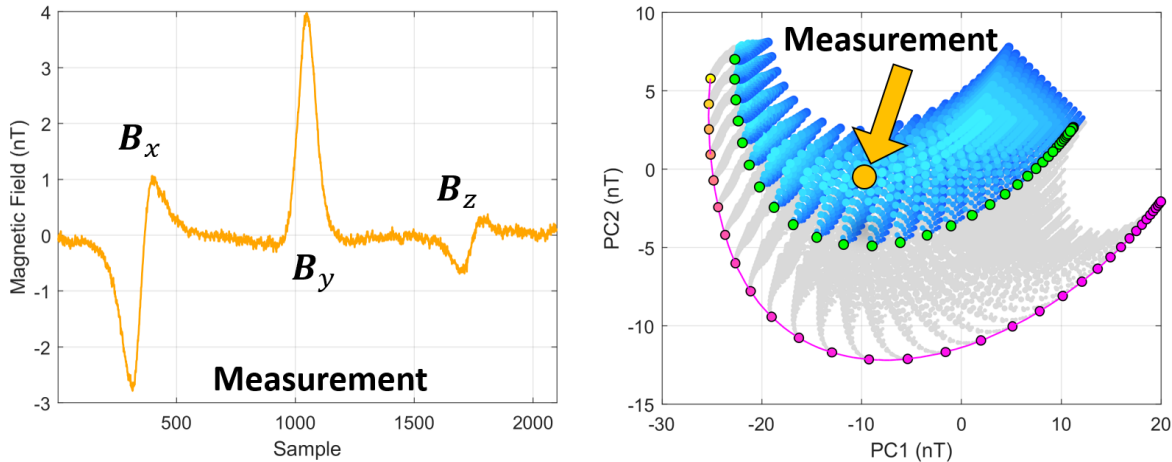


**Figure 11:** Representation of how a measurement gets projected into the PC classification space. (left) A representative noisy measurement of the induced magnetic field from components in concatenated format of an ocean model and (right) depiction of where this measurement gets projected in the PC space defined by the noise-free models.

#### 5.4 Comparison: PCA, Scaled Magnetic Moments, and Total Magnetic Moments

Figure 12 illustrates the classification spaces (only two of three dimensions shown) for PCA, scaled magnetic moments (SMM) and the total magnetic moments (MM), all plotted on the same scale to emphasize the similarities and differences. Also plotted on the same scale are the associated ionospheric magnetic separation plots achieved for each analysis method. As illustrated, the PCA and SMM spaces look very similar and result in identical magnetic separation, which are both scaled compared to the total magnetic moments. As noted earlier, the only difference between PCA and SMM is a rotation of the data space, mainly in PC1 and PC2, which does not impact the magnetic separation between the two model classes.

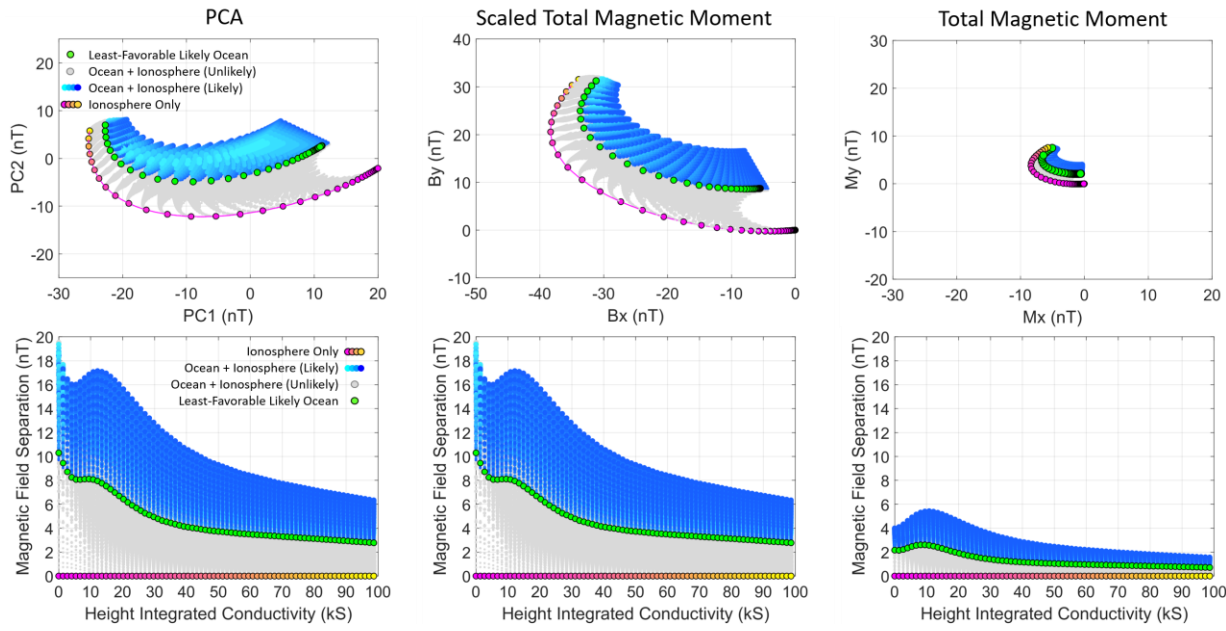
By reducing the dimensionality of the induced dipolar field time-series for both forward modeled data and the actual measurements, PCA allows for easy interpretation of the observations. No information is added or discarded. PCA simply reorganizes the data based on the inherent separation of the scaled magnetic moments, noting that the dipolar matrix is common to all the forward models and the measurement. It can be shown that the projection operation achieved by PCA (using the top three eigenvectors) reduces to a simple 3-by-3 matrix that scales and rotates the magnetic moment vector for each of the  $P$  models. The PCA scaling matrix  $S_{PCA}$  can also be directly related to the eigenvectors and the dipolar matrix as illustrated by,

$$\mathbf{PC}_p = \mathbf{V}'_{PCA} \mathbf{X}_p = \mathbf{V}'_{PCA} (\mathbf{DM}_p) = (\mathbf{V}'_{PCA} \mathbf{D}) \mathbf{M}_p = \mathbf{S}_{PCA} \mathbf{M}_p, \quad (21)$$

and in expanded matrix form illustrated by,

$$\mathbf{PC}_p = \begin{bmatrix} PC_{1,p} \\ PC_{2,p} \\ PC_{3,p} \end{bmatrix} = \begin{bmatrix} v_1(1) & \dots & v_1(3N) \\ v_2(1) & \dots & v_2(3N) \\ v_3(1) & \dots & v_3(3N) \end{bmatrix} \begin{bmatrix} D_{11}(1) & D_{12}(1) & D_{13}(1) \\ \vdots & \vdots & \vdots \\ D_{11}(N) & D_{12}(N) & D_{13}(N) \\ D_{21}(1) & D_{22}(1) & D_{23}(1) \\ \vdots & \vdots & \vdots \\ D_{21}(N) & D_{22}(N) & D_{23}(N) \\ D_{31}(1) & D_{32}(1) & D_{33}(1) \\ \vdots & \vdots & \vdots \\ D_{31}(N) & D_{32}(N) & D_{33}(N) \end{bmatrix} \begin{bmatrix} M_{x,p} \\ M_{y,p} \\ M_{z,p} \end{bmatrix} = \begin{bmatrix} S_{11} & S_{12} & S_{13} \\ S_{21} & S_{22} & S_{23} \\ S_{31} & S_{32} & S_{33} \end{bmatrix} \begin{bmatrix} M_{x,p} \\ M_{y,p} \\ M_{z,p} \end{bmatrix}. \quad (22)$$

794 As previously stated, the scaling matrices in Equations 11-13 ( $\mathbf{S}_{SMM}$ ) and 21 - 22 ( $\mathbf{S}_{PCA}$ ) can be related by a  
 795 translation and a set of rotations.  
 796



797  
 798  
 799 **Figure 12:** PCA provides an enhancement in magnetic separation compared to the total magnetic moments, enabled  
 800 by the retention of all the data. Comparison of the (left panels) PCA, (middle panels) SMM, and (right panels) total  
 801 magnetic moment classification spaces and their associated ocean-to-ionosphere magnetic separation plots. Note  
 802 also that the magnetic separation across the ionosphere HIC range achieved by PCA is identical to that of the SMM.  
 803

## 804 6 Sensitivity to Trajectory and Time-of-Arrival

### 805 6.1 Sensitivity to Trajectory Approach Angle

806 Now that it has been demonstrated that magnetic separation can be increased between the two model classes by  
 807 retaining the signal energy contained in the dipolar field time-series, it is important to further investigate the  
 808 ramifications of a specific trajectory. For the single flyby case, the scaling of both matrices  $\mathbf{S}_{PCA}$  and  $\mathbf{S}_{SMM}$  are  
 809 independent of the magnetic moments and are dependent on the dipolar matrix terms  $\mathbf{D}$  (dictated by the trajectory)  
 810 and the number of samples in the magnetic field time-series. Within limits imposed by signal noise (see Section 7.2),  
 811 magnetic separation can be increased by increasing the number of samples  $N$ . As defined by the dominant diagonal  
 812 scaling terms, an increase in the sample rate by a factor  $K$  results in an increase in the scale factor of  $\sqrt{K}$ . Note that  
 813 reducing the encounter velocity also results in an improved scale factor as more samples can be acquired from the  
 814 magnetometer given the same sampling rate. The dipolar matrix (Equation 8) indicates that reducing the positional  
 815 vector  $\mathbf{r}(t)$  at closest approach also increases the scaling factor as the magnetometer is effectively sampling stronger  
 816 induction fields.  
 817

818 Independent of the scaling matrices associated with the dipolar matrix, the orbital phase of Triton along its highly  
 819 inclined circular orbit (i.e., argument of latitude, AoL) during the spacecraft flyby affects the strength and  
 820 orientation of the magnetic moments as defined in Equation 6. An ideal encounter would occur near the highest or  
 821 lowest position of Triton in its orbit where the 141-hr wave is maximized (see Figure 4), corresponding to an AoL of  
 822 90 or 270°, especially for an ionosphere HIC value above 50,000 S where the 141-hour orbital magnetic wave is the  
 823 primary driver of magnetic induction within the ocean. However, depending on the ocean model and ionosphere  
 824 HIC parameters, the 141-wave maximum magnetic separation can vary as a function of AoL from 50° (higher HIC)  
 825 to 120° (lower HIC) due to the differential phase delay between the two model classes. As discussed in Section 6.2,  
 826 the uncertainty in phase of Neptune's strongest magnetic wave, associated with the 14-hour synodic period, also  
 827 impacts the strength and orientation of the induced magnetic moments. It also dictates the constructive or destructive

interference pattern of the 14-hour and 141-hour total induced magnetic moments (characterized with ionosphere HIC in the range of 0 S to 30,000 S), thus setting constraints on the separability between model classes.

In addition to optimizing the altitude at closest approach, the AoL and approach angle (i.e. latitude and longitude coverage) of the Triton flyby can have an impact on the magnitude of the scaling matrix and the associated magnetic separation between the two model classes. The baseline trajectory (T0) is approximately oriented at a 45-degree angle in the x-y plane of Triton's geographical frame, optimized such that the latitude at closest approach is near 0° where there is the greatest chance to fly over the induced magnetic pole where the field is two times as large as it is at the magnetic equator. (This trajectory is associated with the Trident Concept Study Report, submitted to NASA in November 2020 in response to the Science Mission Directorate's Discovery 2019 Announcement of Opportunity. Trident featured a single flyby by Triton with a specific AoL of 50° and flyby trajectory of ~45°, selected by the Trident team as a joint optimization among multiple science objectives.) To provide guidance for future single or multiple flyby missions, four additional hypothetical trajectories (T1 -T4) were defined to explore the trajectory trade space. These hypothetical trajectories are idealized as straight paths spanning a ±6-minute period about closest approach and are characterized as having the same velocity (18.75 km/s) and altitude (340 km) at closest approach as the baseline trajectory. The AoL is held constant at 50°.

Panel (a) of Figure 13 illustrates the five trajectories T0 – T4 and panels (b) and (c) represents the dipolar matrix coefficients and associated scaling matrices for the baseline (T0) and T1 trajectories, respectively. Panel (d) of the figure illustrates the magnetic separation of the least-favorable likely ocean case with the ionosphere-only models, averaged over all phases of the synodic period and plotted as a function of ionosphere HIC, achieved for all 5 trajectories. Panels (e) and (f) represent the magnetic separation between the least-favorable likely ocean case and the ionosphere models, plotted against ionosphere HIC, for 12 different magnetic phases associated with the Trajectories T0 and T1, respectively. Trajectory T1 is parallel to the y-axis and lies in Triton's equatorial plane (0° latitude). While the baseline (T0) trajectory has a scaling matrix  $\mathbf{S}_{SMM}$  with non-zero mixing coefficients (e.g.  $M_y$  and  $M_z$  feed into  $PC_1$ ), the T1 trajectory yields a purely diagonal scaling matrix  $\mathbf{S}_{SMM}$  where there is no mixing of magnetic moment components. Trajectory T1 is optimal because it has the largest average ocean-to-ionosphere magnetic separation for all ionosphere HIC, due to the relatively large coefficients in the diagonal scaling matrix ( $S_{11}$ ,  $S_{22}$ , and  $S_{33}$ ).

Trajectory T3, which is perpendicular to the Triton equatorial plane, results in very similar performance as T1, indicating that the proposed ocean detection methodology works best when a spacecraft flies through the point in space where T3 and T1 intersect. This occurs because the induced magnetic pole rotates in a plane roughly defined by the geographic equator of Triton where the induced dipolar field is stronger. For the same reason, the T4 trajectory flying over the geographic pole has minimal magnetic separation as the induced magnetic pole is never oriented in this direction, no matter the magnetic phase of Neptune.

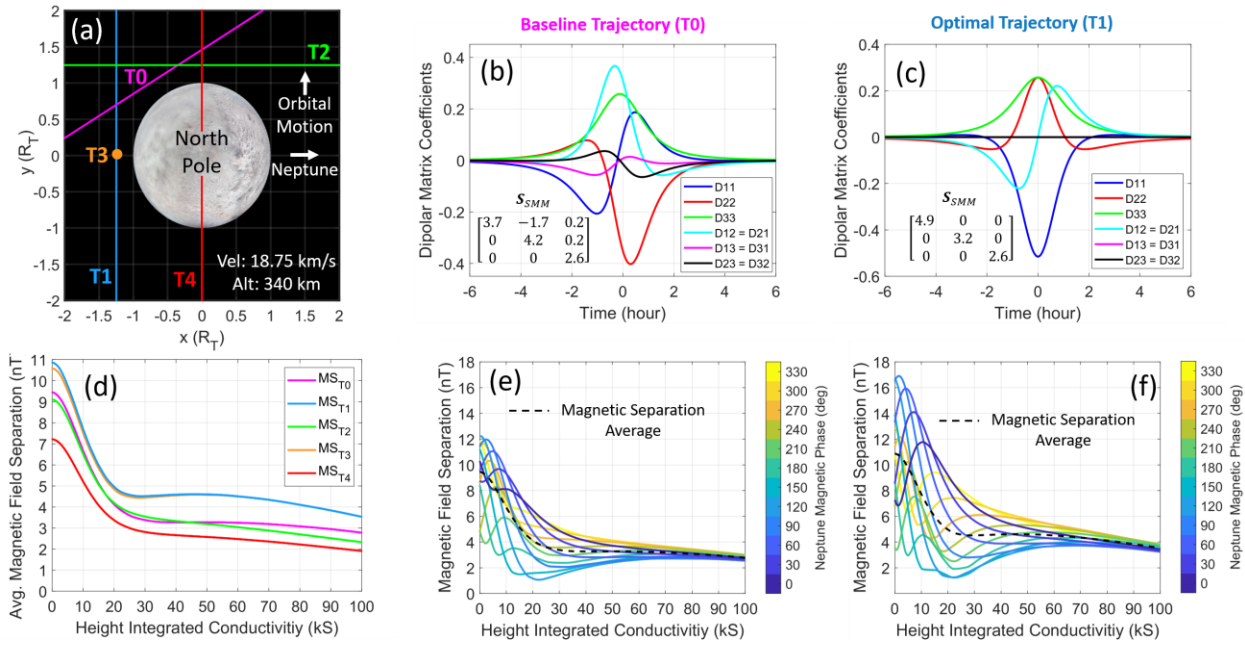


**Figure 13: Magnetic separation of ocean-to-ionosphere PCs is influenced by the trajectory.** (a) Comparison of 5 different flyby trajectory geometries. Note that T3 is perpendicular to the 2D image and comes out of the page. T1, and T2 are located in Triton's equatorial plane. T0 has a slight dependence on  $z$ , but CA is at zero longitude. T4 has a Triton latitude of  $90^\circ$  and CA is over the North Pole. (b,c) Dipolar matrix coefficients as a function of time for the baseline trajectory (T0) and optimal trajectory (T1), respectively. (d) Magnetic separation averaged across all magnetic phases of Neptune's 14-hr synodic wave as a function of ionosphere HIC for the 5 different trajectories illustrated in (a). (e,f) Ocean-to-ionosphere magnetic separation of the least-favorable likely oceans as a function of ionosphere HIC for various phases of Neptune's 14-hr synodic wave for the baseline trajectory (T0) and optimal trajectory (T1), respectively

## 6.2 Sensitivity to Unknown Phase of 14-hour Wave

The phase of Neptune's 14-hour magnetic wave will be unknown prior to the arrival of a future spacecraft. Thus, new measurements will be required in Neptune's magnetosphere to update the existing field model to accurately account for magnetic phase in the spherical harmonic coefficients. This phase uncertainty has implications on the total magnetic moments for a single encounter based on the constructive and destructive interference with the 141-hour orbital magnetic wave. Any proposed Triton ocean-detection methodology must account for the unknown 14-hour magnetic phase at arrival in the Neptune system. The method described in this paper has been extensively analyzed to assure confident ocean detection for any 14-hour magnetic wave phase possibility. To simulate a different magnetic phase  $\varphi$  with respect to the existing magnetic field model of Neptune for a given instance in time, the spherical harmonic coefficients are modified by

$$\tilde{g}_n^m = g_n^m \cos(m\varphi) - h_n^m \sin(m\varphi), \quad (23)$$

$$\tilde{h}_n^m = h_n^m \cos(m\varphi) + g_n^m \sin(m\varphi), \quad (24)$$

and the magnetic field is recomputed using Equation 1 with the modified coefficients.

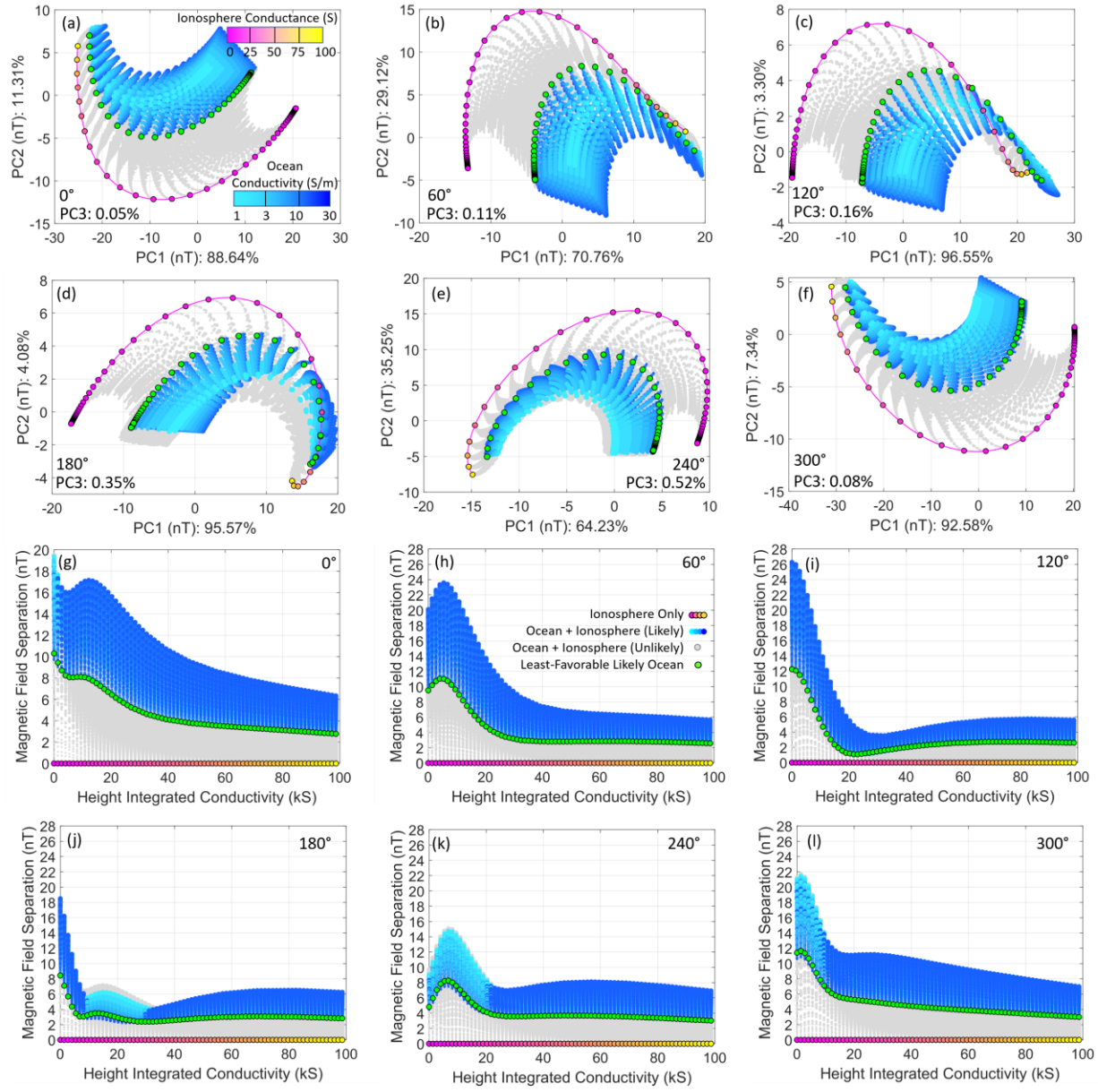
As the 14-hour magnetic phase varies from  $0^\circ$  to  $360^\circ$ , the magnetic moments and scaled magnetic moment ocean classification spaces, derived from Equation 17, also rotate by  $360^\circ$  (primarily in  $M_x$  and  $M_y$ ) where the lowest intensity ionosphere-only model is located at the origin (i.e., no magnetic induction response). Within this  $360^\circ$  rotation range, the location of the ionosphere only models with respect to the ocean-plus-ionosphere can vary, appearing to cross over and intersect in a 2-dimensional space, thus reducing the magnetic separation for certain phases of the synodic wave, but still maintaining model class isolation when viewed in the 3rd dimension. This

reduction in magnetic separation occurs when the phase of the synodic wave is roughly in the range from 90° to 180° (noting phase is relative to the Connerney et al., 1991 magnetic field model). Because the PCA eigenvectors align the data along the PCs of greatest variance, the classification space does not perfectly rotate as the magnetic moments or scaled magnetic moments for different phases of the synodic period. This is illustrated in panels (a)-(f) of Figure 16 where the 14-hour magnetic phase has been varied in increments of 60°. The associated magnetic separation between model class achieved by PCA is plotted as a function of ionosphere HIC in panels (g)-(l) of Figure 16. The worst-case scenario occurs when the phase of the 14-hour wave is near 120° and when the ionosphere HIC is in the range of 15 kS to 25 kS. Although it appears that some of the ionosphere-only models overlap with the ocean-plus-ionosphere models, the 3<sup>rd</sup> dimension (PC<sub>3</sub> not shown) provides enough magnetic separation to fully isolate the two classes of data (green circles) by at least 1-nT.

To improve separability, if required for such a worst-case scenario (e.g., 120° magnetic phase), the 14-hour wave's dipole magnetic field contribution to the time-series can be mathematically removed from the forward modeled data. More specifically, the PC classification space is recomputed with a modified set of data defined by  $\mathbf{B}_{ind}(t) - \mathbf{B}_{ind,14RM}(t)$ , where the latter term represents the dipolar magnetic field time series associated with the 14-hour wave for a single selected reference model (RM) with the associated magnetic moment,

$$\mathbf{M}_{14RM}(t) = -A_{14RM} e^{-i\phi_{14RM}} \mathbf{B}_{N,14RM}(t), \quad (25)$$

where the  $A_{14RM}$  is the amplitude and  $\phi_{14RM}$  is the phase delay of the selected reference model. Note that use of a single reference model does not – and need not – completely remove the 14-hour dipolar field contribution exactly for all models. Instead, it transforms the PC space into one that effectively provides a partially removed 14-hour wave, which is shown to still be adequate. Once the actual measurement is acquired, prior to projection into the altered PC space using the updated eigenvectors, the dipolar magnetic field time series associated with the 14-hour wave reference  $\mathbf{B}_{Ind,14M}(t)$  is removed from the noisy measurement. Because the same reference model is removed from the forward modeled data and the measurement, no error is introduced by this process. Note also that this model subtraction method would only rarely be necessary; specifically, only when all the following conditions are met: 1) a hard-to-detect ocean (thin and with low-conductivity) is present, 2) ionosphere HIC is in the range 15 kS – 25 kS, and 3) Neptune's magnetic phase happens to be near 120° with respect to the Connerney et al., (1991) field model. When the ionosphere HIC is greater than 30 kS, the 14-hour wave becomes less influential as it does not have the ability to penetrate the highly conducting ionosphere; the magnetic separation is minimally affected by the variation of phase of this wave. As will be demonstrated in the next section, this subtraction technique would not be required in a multi-pass mission, as PCA can combine the measurement data sets from each encounter for improved magnetic separation.



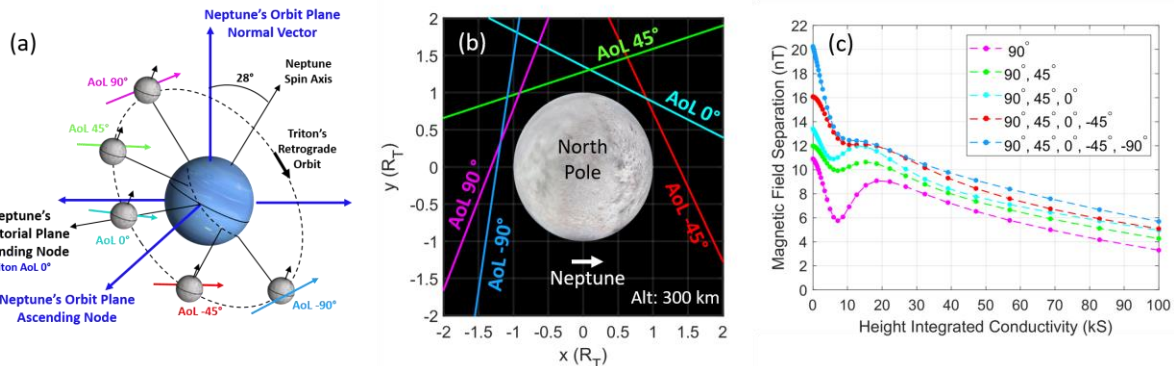
935  
936  
937  
938  
939  
940  
941  
942  
943  
944  
945  
946  
947  
948  
949  
950

**Figure 16:** Magnetic separation of ocean-to-ionosphere models depends on the phase of Neptune's synodic wave which will be unknown prior to arrival. Panels (a) - (f) comparison of the PC space (2 of 3 dimensions shown) for various magnetic phases of Neptune at increments of  $60^\circ$  relative to the  $0^\circ$  Connerney et al. (1991) model baseline. Note that the majority of the variance is explained by PC1 and PC2 as indicated by the labels of each axis; however, there is a third principal axis (not shown in these plots) that in this analysis is very important, as it is useful in separating the ocean and ionosphere models which appear to overlap for magnetic phases in the range from  $90^\circ$  to  $180^\circ$ . Panels (g) - (l) Ocean-to-ionosphere magnetic separation plots versus ionosphere HIC for the 3-dimensional PC spaces illustrated in panels (a)-(f). Note that for the most likely oceans (those ocean cases above the green-colored models), complete separability is achieved between all ionosphere models. The best-case Neptune magnetic phase for ionosphere HIC in the range of 0 to 10 kS corresponds to  $120^\circ$ , coincidentally the worst-case magnetic separation for ionosphere HIC is in the range of 20 kS to 30 kS. In this latter HIC region, the least-favorable likely ocean case, represented by the green circles, is separated from the ionosphere models by 1 nT which is sufficient as dictated by the noise analysis presented in Section 7.2.

### 951 6.3 Sensitivity to Multiple Encounters

952 Although the discussion so far has been limited to applicability of the method for a single flyby, the PCA ocean  
 953 detection (and characterization) approach is not restricted to a single encounter and can easily be adapted for a  
 954 multi-flyby orbiter mission. PCA affords additional advantages to multi-pass orbiter missions, beyond that delivered  
 955 for a single flyby, when multi-sets of magnetic induction fields are concatenated into a single input matrix. The PCA  
 956 ocean detection methodology allows data from a series of passes or flybys to be concatenated, similar to how the  
 957 magnetometer channels were concatenated for a single flyby, into a single input design matrix. As an example, panel  
 958 (a)-(b) of Figure 14 illustrates five separate hypothetical trajectories associated with five different positions of Triton  
 959 along its inclined orbit ( $AoL = +90^\circ, +45^\circ, 0^\circ, -45^\circ, -90^\circ$ ). Panel (c) of Figure 14 illustrates the associated magnetic  
 960 separation for the least-favorable likely ocean cases (50 km ocean thickness and 9 S/m conductivity), beginning with  
 961  $AoL$  of  $+90^\circ$ , for one-, two-, three-, four-, and five-flyby scenarios.

962 When magnetic field datasets from multiple trajectories are concatenated and used as input into PCA, the  
 963 eigenvectors expand from a vector length of  $3N$  to  $6N$  for two flybys, to  $9N$  for three flybys, and so on. New  
 964 information is contained within the data acquired from these additional flybys including variation in trajectory angle  
 965 with respect to the direction of Neptune (change in dipolar matrix), the trajectory velocity which impacts the number  
 966 of samples used for processing, and the change in magnetic moments associated with the variation in the driving  
 967 magnetic fields. PCA maximizes the variance in this larger dataset, thereby resulting in a set of eigenvectors (3 by  
 968  $15N$  in the case for 5 flybys) that yield a set of new PCs. The additional information presented to the algorithm  
 969 results in improved magnetic separation compared to that achieved from a single flyby mission as it maximizes that  
 970 data variance across all passes. As a result, the method has the ability to tighten constraints for ocean  
 971 characterization as described in Section 9.



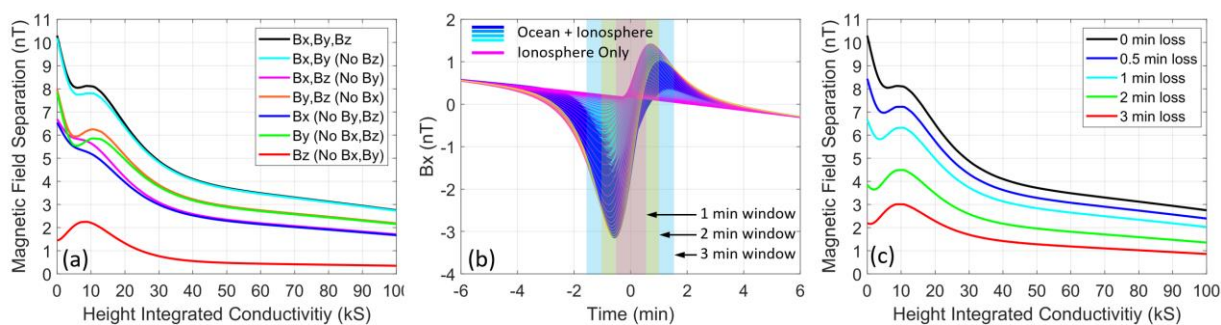
974 **Figure 14:** Magnetic separation, and hence classification margin, can be improved with added encounters. (a)-(b)  
 975 Comparison of 5 different available single-pass trajectories (developed under Trident) corresponding to times when  
 976 Triton is at  $AoL$  of  $+90^\circ, +45^\circ, 0^\circ, -45^\circ, -90^\circ$  and (c) the corresponding least-favorable likely ocean-to-ionosphere  
 977 magnetic separation as a function of ionosphere HIC for one- (starting with  $AoL$  of  $90^\circ$ ), two-, three-, four-, and  
 978 five-flyby scenarios.

## 981 7 Sensitivity to Noise and Error Sources

### 982 7.1 Sensitivity to Loss of Data

983 PCA also affords additional flexibility of ocean detection in the event of various forms of data loss. One such  
 984 example is when measurement data for one or even two of the magnetometer channels may be lost, corrupted, or  
 985 intentionally dropped due to large magnetic field perturbations generated by the moon's plasma interaction. While  
 986 this would reduce ocean-to-ionosphere magnetic separation, there is no constraint that all three magnetometer  
 987 channels must be used to form the design matrix  $\mathbf{X}$  (Equation 18b). Panel (a) of Figure 15 illustrates, for the baseline  
 988 trajectory T0, the sensitivity of magnetic separation for the least-favorable bounding ocean case when various  
 989 magnetometer channels are dropped. Figure 15 demonstrates that ocean detection is still possible as long as  $B_x$   
 990 and/or  $B_y$  is retained. The  $B_z$  component contains very little information and is not well suited for ocean detection  
 991 alone. The PCA-based approach also demonstrates robustness against unintentional full channel outages and

992 resiliency against temporary data loss. Panels (b) and (c) of Figure 15 illustrate the effect on magnetic separation for  
 993 0.5, 1, 2, and 3-minute data dropouts in all three magnetometer channels, centered around closest approach.  
 994 Flexibility is also provided to selectively drop small windows of data at closest approach if the measurement is  
 995 subsequently found to contain higher order moment induction signatures (e.g., from asymmetric ocean or  
 996 ionosphere) near the surface not included in the forward modeling.  
 997



1000 **Figure 15:** PCA is robust to various forms of data loss. (a) Comparison of the ocean-to-ionosphere magnetic  
 1001 separation for the least-favorable likely ocean as a function of ionosphere HIC resulting from different  
 1002 combinations of the three magnetometer channels being used by PCA. (b) Illustration depicting different windows of  
 1003 data loss in all channels (only  $B_x$  channel shown) and (c) the ocean-to-ionosphere magnetic separation for the least-  
 1004 favorable likely ocean as a function of ionosphere HIC for each of the data loss cases illustrated in (b).

## 7.2 Sensitivity to Random and Structural Noise

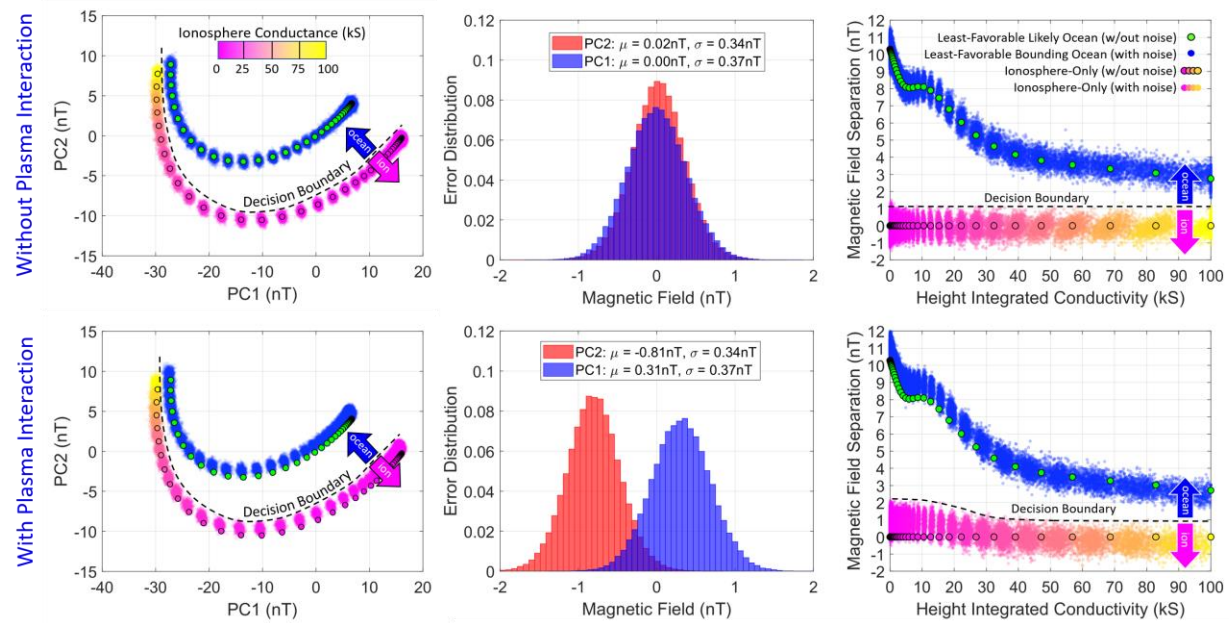
A Monte Carlo simulation involving all of the ionosphere-only models (51 models) and the associated least-favorable likely ocean cases (51 models) was performed to demonstrate the robustness of the methodology when faced with various patterns of noise. A set of 1,000 simulated flybys with different noise characteristics was simulated for each of the 102 models, assuming a magnetic phase of  $0^\circ$ . The instrument noise model used was based on the performance of a fluxgate magnetometer having an electronics white noise of 30 pT and sensor flicker noise characterized with 30 pT at 1-Hz and 300 pT at 1-mHz.

The spacecraft error sources (held constant for each of the 1,000 flybys) include a  $1^\circ$  ( $3\sigma$ ) attitude uncertainty in each axis, 1 ( $3\sigma$ ) second timing error, and 10 km ( $3\sigma$ ) position uncertainty in each dimension. A DC offset error was also introduced into the measurements (also held constant) with 0.1 nT ( $3\sigma$ ) uncertainty, representing the *residual offset* residing in each axis after in-flight calibration retrieval of the undistinguishable stray spacecraft fields, fluxgate sensor offsets, and electronics offsets. A deviation in the complex response function (amplitude and phase delay) by 1% ( $3\sigma$ ) for each magnetic wave at the various frequencies in the simulated measurements was included in the analysis to account for modeling unknowns.

Coincidentally for the trajectory used for this paper, the magnetic phase of  $0^\circ$  established in the baseline Connerney et al., (1991) model corresponds to a spacecraft time-of-arrival when Triton is crossing Neptune's magnetic equator, where plasma density is anticipated to be at a maximum. To ensure PCA's robustness against plasma interaction fields, the plasma density of the current sheet assumes 10 times the density of what Voyager encountered. However, hybrid modeling described in Liuzzo et al. (2021) reveals that the plasma interaction fields are relatively small for the baseline trajectory when Triton is at an AoL of  $50^\circ$  (see Figure 5) due to the favorable magnetic field -plasma flow angle. Even at other AoLs, the maximum magnetic field perturbations generated by the plasma interaction are only on the order of 1 nT (see Figures 4 and 6 in Liuzzo et al., 2021); however, these occur when Triton is many Neptune radii away from the plasma sheet where the plasma densities are expected to be much lower than those simulated. Thus, for the purposes of this analysis, there is no need to remove the modeled plasma interaction field effects from the magnetic field measurements. Instead, the plasma effects are absorbed as a tolerable structured noise source. Table A2 in the Appendix provides a more detailed summary of the noise and error sources included in this analysis.

1036 After simulating 1,000 flybys for each of the ionosphere-only and ocean-plus-ionosphere models, PCA is used to  
 1037 project the noisy data into the PC classification space as defined in Equation 20. Figure 17 illustrates the results of  
 1038 the PC space, PC error distribution, and PC ionosphere-to-ocean separation distance of the Monte Carlo simulations  
 1039 with inclusion of the various noise sources. The top three panels are associated with the simulation that does not  
 1040 include the plasma induced effects and the bottom panels include them. As illustrated in the PC space for both cases,  
 1041 the noise alters the absolute position of a model in the PC space depending on the ionosphere intensity (here shown  
 1042 in two dimensions). In the plasma-free case, each simulated measurement is projected into the classification space  
 1043 within a *noise sphere* with  $3\sigma$  radius of roughly 1 nT, corresponding to the PC error distributions (middle panels).  
 1044 Positive ocean detection occurs if the PCA projected measurement falls on the ocean side of the decision boundary  
 1045 defined in the figure.

1046 When the plasma-induced fields are included, the simulated measurements also are projected into a region  
 1047 defined by a 1 nT noise sphere. However, in this case, the plasma interaction fields have the effect of offsetting the  
 1048 sphere's position. Here, the models have their PC1 shifted by 0.31 nT and their PC2 shifted by 0.81 nT. Because the  
 1049 offsets for each axis are different and the ocean decision boundary shares multiple dimensions, the boundary is  
 1050 modified and takes on an ionospheric HIC dependence as illustrated in the bottom right plot of Figure 17. Note that  
 1051 the relative separation between all ocean models and their corresponding ionospheres is preserved, but their absolute  
 1052 position is not. Because of this, the decision boundary is raised to 2 nT (with respect to the noise-free ionosphere  
 1053 models for ionospheres characterized with  $HIC < 20$  kS), but the 1 nT level boundary for ionosphere HIC greater  
 1054 than 20 kS is maintained to ensure proper classification when plasma effects are not assumed to be present. Note  
 1055 that the reduction of magnetic separation between ocean and no-ocean models with ionosphere  $HIC < 20$  kS is not a  
 1056 concern as there is already large separation due to the impact of the stronger 14-hour wave. As mentioned above,  
 1057 plasma-induced fields are treated as a noise source in this analysis. No attempt is made to model and remove their  
 1058 impact as their presence is tolerable to the method especially when the low probability of the plasma current sheet  
 1059 being sufficiently close to Triton is considered. However, if by chance the plasma-induced currents happen to be  
 1060 unexpectedly larger than anticipated, they can be modeled (see Liuzzo et al 2021) and then partially removed prior  
 1061 to classification.



1063  
 1064 **Figure 17:** The proposed method is robust to various noise sources. Monte Carlo simulation results are shown with  
 1065 various sources of noise described in the text (top row) without and (bottom row) with plasma interaction fields  
 1066 present. The left two panels represent the PC space for both simulations, the middle panels represent the absolute  
 1067 PC position error (for largest two components) extracted from the simulated measurements, and the right panels  
 1068 illustrate the separation distance of the models, projected into a 2-dimensional space as a function of ionosphere  
 1069 HIC.

## 1070    8 Detectable Oceans for a Single-Pass Trajectory

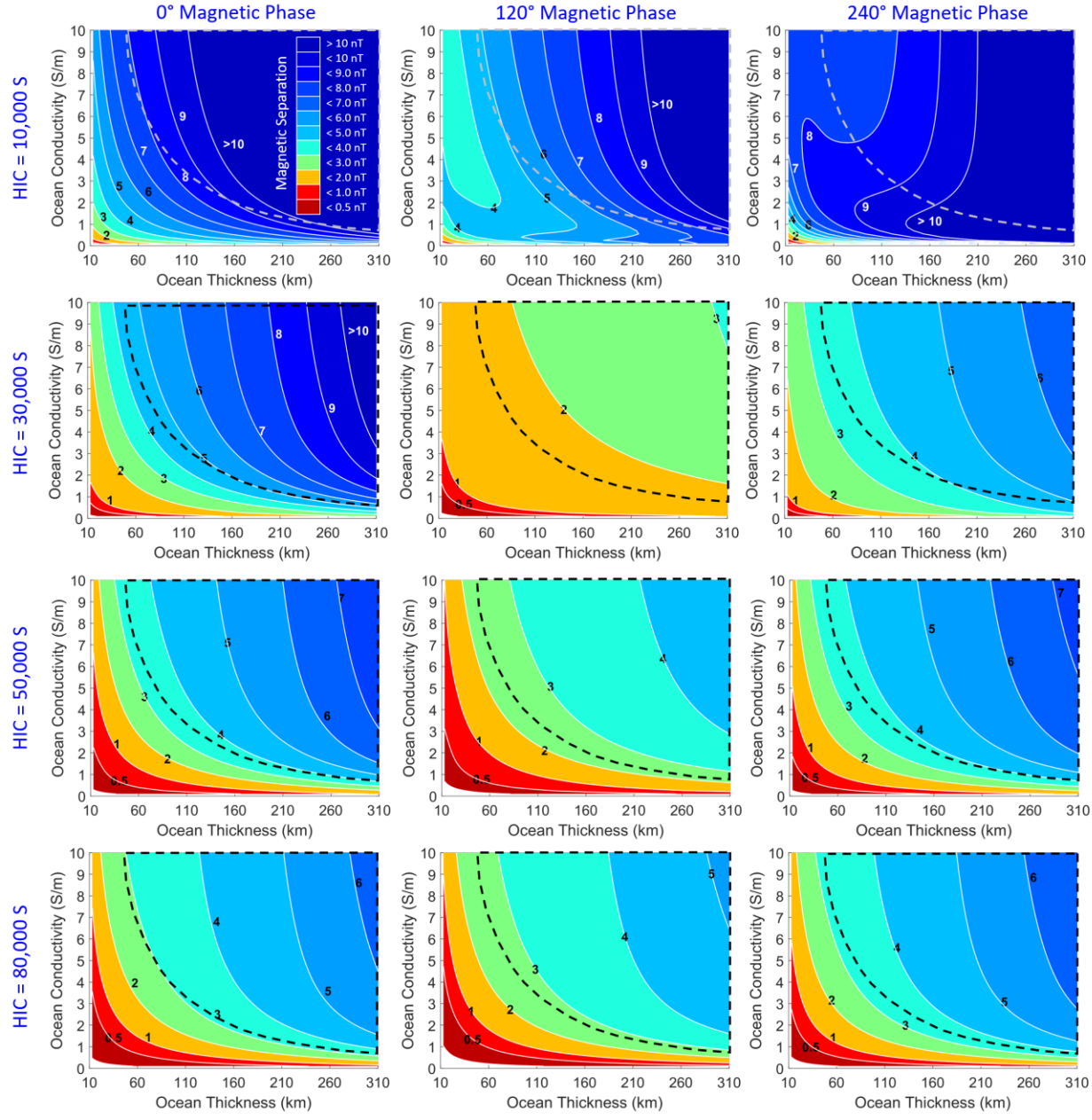
1071  
1072 For a single flyby mission, the confidence in the detection of a potential sub-surface ocean increases with increased  
1073 magnetic separation of the model classes in the ocean classification space. For a given ionosphere HIC and 14-hour  
1074 magnetic phase, magnetic separation varies as a function of the ocean model's physical attributes. The thickness of  
1075 the ice shell strongly influences the magnetic separation because of the  $1/r^3$  dipole falloff associated with the ocean's  
1076 depth below Triton's surface. Oceans with less conductivity also have a smaller induction response to Neptune's  
1077 driving magnetic waves. Figure 18 illustrates the ocean-to-ionosphere magnetic separation contours as a function of  
1078 ocean thickness and ocean conductivity for 12 different scenarios corresponding to different combinations of  
1079 Neptune's 14-hour magnetic phase and ionosphere HIC. Note that only models with ocean conductivity of 10 S/m or  
1080 less are shown for clarity. Superimposed on each of the 12 panels is a black dashed contour region highlighting the  
1081 most likely ocean cases, consistent with Figure 6.

1082 From the noise analysis results in Section 7, it was determined that any ocean-plus-ionosphere model that is  
1083 spaced within 1-nT of an ionosphere-only model is indistinguishable from each other and therefore cannot be  
1084 positively labeled as ocean with certainty. In Figure 18, this indistinguishable region is represented by the red  
1085 contour and represents the ocean models that cannot be definitely be detected. The worst-case magnetic separation  
1086 of the dataset shown occurs when the magnetic phase is 120° and the ionosphere HIC is 30 kS. In this case, all of the  
1087 most likely ocean models (contained within the dashed line) are detectable with at least 2-nT of magnetic separation  
1088 from the ionosphere-only model. Note that for each of the datasets with ionosphere HIC of 50 kS and above, the  
1089 contours for any given magnetic phase of the synodic period look similar as this wave is attenuated by the high  
1090 ionospheric conductance, and therefore plays less of a role in magnetic induction within the ocean. This dataset  
1091 indicates that even for a single encounter using the baseline trajectory, a large ocean parameter space can be  
1092 uniquely differentiated from an ionosphere response, even in the presence of various sources of noise and a highly  
1093 conducting ionosphere.

1094

1095

1096



1097  
 1098  
 1099 **Figure 18:** Dependence of ocean-to-ionosphere magnetic separation for range of ionosphere HIC and Neptune  
 1100 magnetic phase for a single-flyby. Each panel represents the magnetic separation contours (units of nT) of the  
 1101 ocean-plus-ionosphere models from the ionosphere-only models as a function of ocean thickness and ocean  
 1102 conductivity for (left column) magnetic phase of 0°, (middle column) worst-case magnetic phase of 120°, and (right  
 1103 column) 240°, for ionosphere HIC of 10 kS, 30 kS, 50 kS, and 80 kS. Black dashed region highlights the most likely  
 1104 ocean space (§2.3). The red contours indicate magnetic separation below 1nT where ocean classification or  
 1105 differentiation could not be performed with certainty.  
 1106  
 1107  
 1108  
 1109  
 1110

## 1111 9 Ocean and Ionosphere Characterization for a Multi-Pass Trajectory

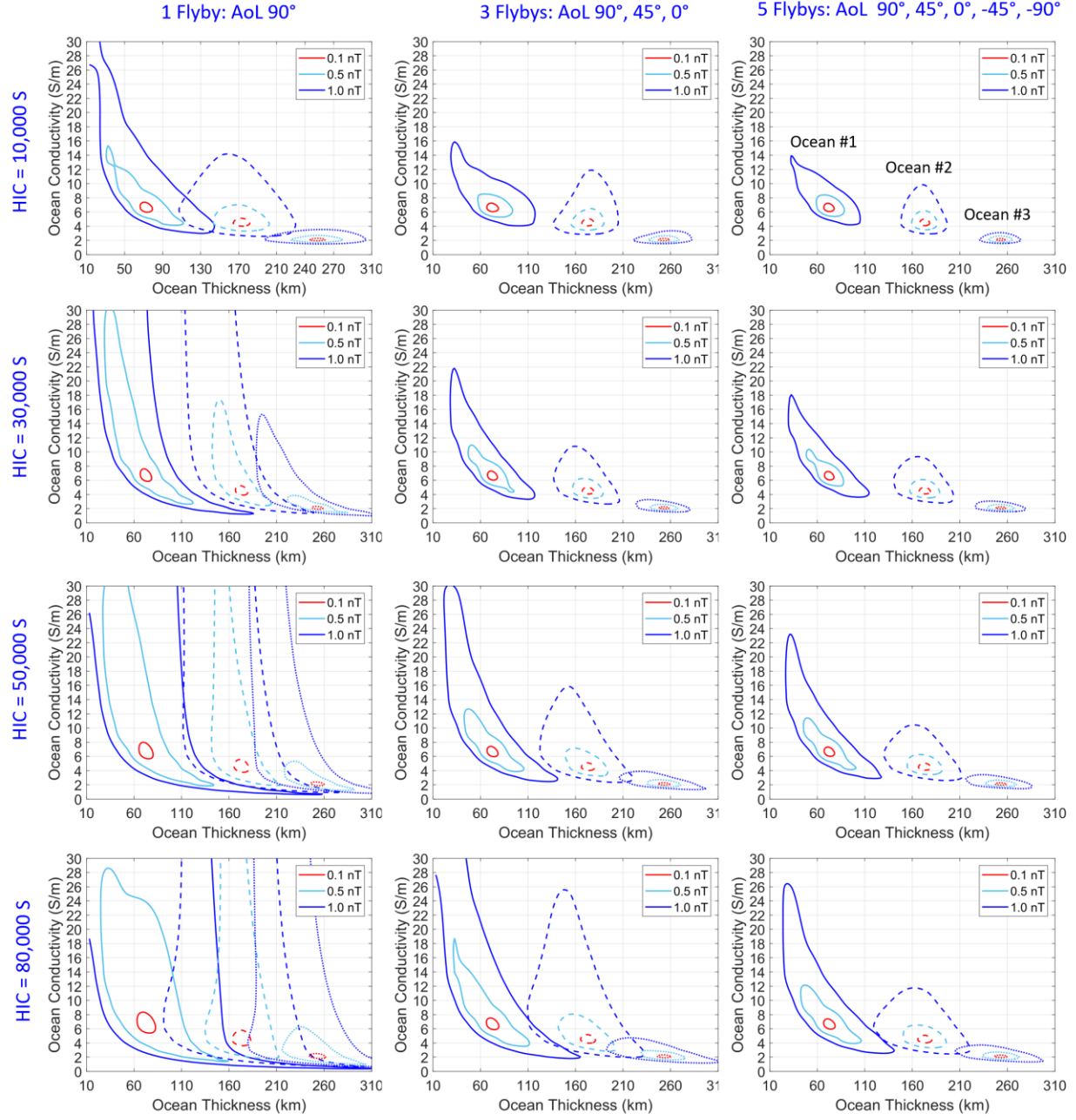
1112  
1113 The method described in this paper is not only able to distinguish the induction response of an ocean-plus-  
1114 ionosphere from that of an ionosphere-only response, but it can also characterize the interior profile based on where  
1115 the projected measurement lands in the 3-dimensional classification space. The spatial location of the projection  
1116 provides an estimate of the ocean conductivity and thickness as well as the ionosphere conductance. The panels of  
1117 Figure 19 illustrate characterization contours associated with three representative oceans for a single flyby (column  
1118 1), three flybys (column 2), and five flybys (column 3), for four different ionosphere HIC values (rows). The  
1119 contour boundaries, owing to three different levels of noise (1 nT, 0.5 nT, and 0.1 nT), encompass the ocean models  
1120 that are indistinguishable from the underlying ocean. The assumed noise dictates the uncertainty of model  
1121 parameters, thereby setting constraints on characterization of the ocean thickness and conductivity. As illustrated,  
1122 the ocean thickness and conductivity of a putative subsurface ocean at Triton can be broadly constrained for a single  
1123 flyby. However, as more flybys are added, ocean-to-ionosphere and ocean-to-ocean model separation distances  
1124 increase (See Section 6.3), hence tightening the precision of the estimated parameters of the underlying oceans. As  
1125 the ocean thickness decreases and the surface depth increases, ocean conductivity becomes more difficult to discern.  
1126 Estimates of ocean conductivities and ocean thicknesses improve with multiple flybys across the entire ionosphere  
1127 intensity range, including HIC levels above 50,000 S where the 14-hour wave has less ability to penetrate the  
1128 ionosphere and contribute to induction.

1129

1130

1131

1132



1133  
1134  
1135  
1136  
1137  
1138  
1139  
1140  
1141  
1142  
1143  
1144

**Figure 19:** Measurements from multiple flybys can be used to improve confidence in estimation of ocean parameters. Each panel in the figure illustrates characterization contours of three representative oceans for (left column) one flyby at AoL of  $+90^\circ$ , (middle column) three flybys at AoL of  $+90^\circ$ ,  $+45^\circ$  and  $0^\circ$  and (right column) five flybys at AoL of  $+90^\circ$ ,  $+45^\circ$ ,  $0^\circ$ ,  $-45^\circ$ , and  $-90^\circ$ , where each row corresponds to a different ionosphere HIC scenario. Ocean #1 ( $T_o = 75$  km,  $\sigma = 6.5$  S/m) is represented by the solid lines, ocean #2 ( $T_o = 175$  km,  $\sigma = 4.5$  S/m) is represented by the dashed lines, and ocean #3 ( $T_o = 255$  km,  $\sigma = 2.0$  S/m) is represented by the dotted lines. The three contours shown for each ocean represent the boundaries that encompass the indistinguishable oceans when three different levels of noise are considered (blue = 1 nT, cyan = 0.5 nT, and red = 0.1 nT).

## 1145 10 Conclusions

1146  
 1147 Increasing scientific interest in ocean worlds highlights the need for advances in analytic techniques to positively  
 1148 determine the presence of subsurface oceans in challenging environments. The principal component analysis (PCA)  
 1149 based analysis method described in this paper represents a new paradigm for processing space-based magnetometer  
 1150 measurements, with demonstrated advantages in reliably distinguishing the presence and key characteristics of a  
 1151 conductive liquid layer even in the face of the confounding factors of a conductive ionosphere, local plasma  
 1152 interaction currents, systemic uncertainties, and various noise and error sources. Unique features of the PCA method  
 1153 provide additional advantages of flexibility and resiliency. Magnetic separation between the ocean-plus-ionosphere  
 1154 and ionosphere-only model classes is enhanced and sufficiently maintained even with incomplete input data, while  
 1155 flexibility to pre-select measurement data channels or data time intervals for inclusion in the PCA input data set  
 1156 enables selective removal of contaminated data if necessary. Using Neptune's largest moon Triton as an example  
 1157 ocean world, PCA was directly applied to a three-axis magnetic induction field dataset and shown to be a powerful  
 1158 ocean classification tool, distinguishing the induced magnetic responses of ionosphere-only cases from those of the  
 1159 ionospheres convolved with candidate potential oceans, even on a single flyby. The flexibility and extensibility  
 1160 afforded by the PCA-based method enhance the existing and future capabilities for ocean detection and  
 1161 characterization at candidate ocean worlds throughout the solar system.

## 1162 Methods

1163 For all timing and ephemeris computation in this work, the NAIF developed SPICE toolkit for Matlab called mice  
 1164 ([https://naif.jpl.nasa.gov/naif/toolkit\\_MATLAB.html](https://naif.jpl.nasa.gov/naif/toolkit_MATLAB.html)) was utilized. All magnetic field models and field line visuals  
 1165 were implemented in MATLAB. The most recent kernel files (pck00010.tpc, naif0012.tls, de435.bsp, de431.tpc,  
 1166 nep081.bsp, nep095.bsp) were leveraged and all IAU defined reference frames defined in the IAU working group  
 1167 report (Archinal et al., 2018) were used.

## 1168 Acknowledgements

1169 The authors thank Krishan Khurana of UCLA for fruitful discussions on magnetic induction and plasma interaction  
 1170 at Triton, Michael Turmon of JPL for his insights into the PCA ocean detection approach and Try Lam of JPL for  
 1171 the design of the trajectories used in this work.

1172  
 1173 The research was carried out at the Jet Propulsion Laboratory, California Institute of Technology, under a contract  
 1174 with the National Aeronautics and Space Administration (80NM0018D0004). Funding support was provided by the  
 1175 NASA Discovery Program, as part of the Trident mission Phase A study (80NM0020F0034).

## 1176 Data Availability Statement

1177 The data contained in this publication are archived on Zenodo at doi.org/10.5281/zenodo.5484442. The data are  
 1178 stored in Matlab.mat structure files with an associated .m script for easy data extraction. Currently, the data is  
 1179 restricted access until publication. The reviewers and editors will have access to the dataset which is temporarily  
 1180 stored at the following link <https://drive.google.com/file/d/1neSaxprad9oYHZusAShfWlvGPd--IdT4/view?usp=sharing>

## 1183 Appendix

1184

Label	Frequency (μHz)	Period (hr)	Bx (nT)	By (nT)	Bz (nT)
DC	0	-	0.2057	0.009	-3.0633
f <sub>s</sub>	19.2125	14.4582	6.7834	3.4094	0.3759
f <sub>o</sub>	1.9694	141.0457	2.574	1.2847	0.189
2f <sub>s</sub>	38.4250	7.2291	0.2563	0.1713	0.0092
3f <sub>s</sub>	57.6375	4.8194	0.0042	0.0032	0.0001
2f <sub>o</sub>	3.9388	70.5229	0.0593	0.0394	0.0067
f <sub>s</sub> - f <sub>o</sub>	17.2431	16.1095	0.2481	0.0122	1.3562

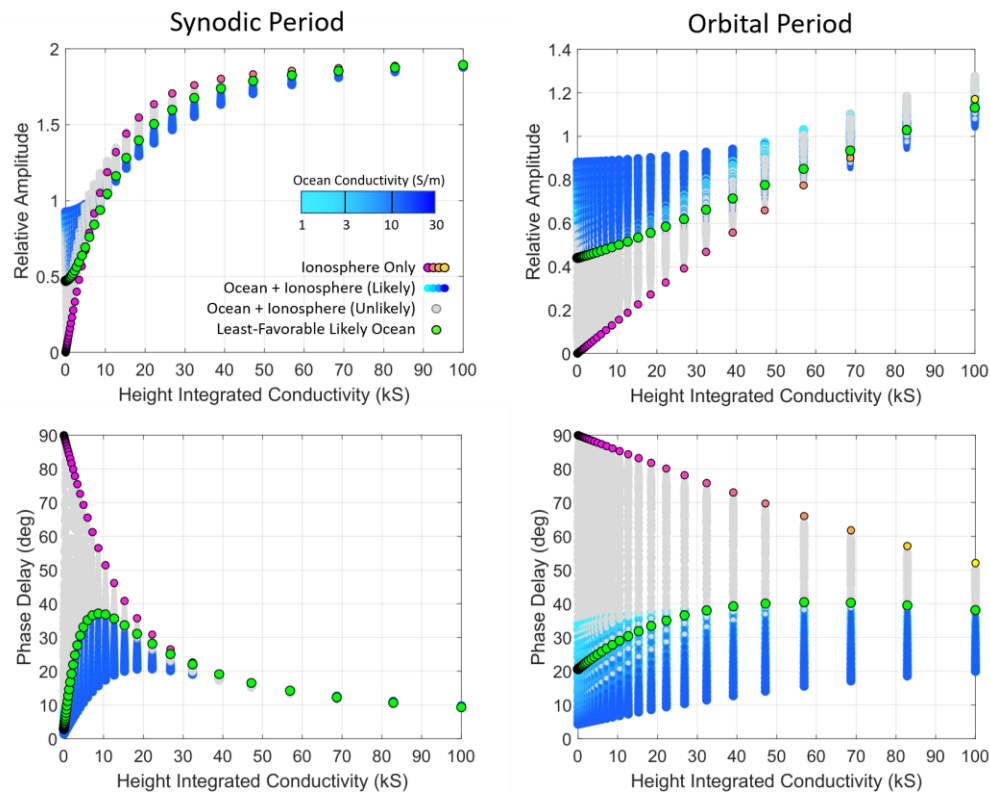
fs + fo	21.1819	13.1139	0.2568	0.1714	0.0088
fs - 2fo	15.2737	18.1867	0.2697	0.1362	0.0513
fs + 2fo	23.1513	11.9983	0.0041	0.003	0.0002
fs - 3fo	13.3043	20.8789	0.0107	0.0069	0.0008
fs + 3fo	25.1208	11.0577	0.0002	0	0
2fs - fo	36.4556	7.6196	0.0085	0.0022	0.0687
2fs + fo	40.3944	6.8766	0.009	0.0068	0.0002
2fs - 2fo	34.4862	8.0548	0.0205	0.001	0.0027
2fs + 2fo	42.3638	6.5570	0.0002	0.0001	0.0001

1185  
1186  
1187  
1188  
1189**Table A1.** List of the frequencies and amplitudes of the magnetic waves encountered by Triton. fs represents the synodic frequency and fo represents the orbital frequency.

Measurement Error Source	Error Parameter	Error Value
Spacecraft Ephemeris Uncertainty	Attitude uncertainty (all axes)	+/- 1° (3σ)
	Timing uncertainty	+/- 1 sec (3σ)
	Position uncertainty (all axes)	+/- 10 km (3σ)
Instrument Noise	Electronics White Noise	30 nT
	Sensor Flicker Noise	30 nT @ 1Hz 300 nT @ 1mHz
Deviation in Complex Response Function	Amplitude deviation (all frequencies)	+/- 1% (3σ)
	Phase deviation (all frequencies)	+/- 1% (3σ)
DC Level (Residual after Offset Calibration)  Plasma Interaction Fields	Spacecraft field, sensor offset	+/- 0.1 nT (3σ)
	Plasma Density	Electrons: 0.03 - 0.11 cm <sup>-3</sup> Ions: 0.03 - 0.11 cm <sup>-3</sup>
	Plasma Temperature	30 eV electrons 65 eV ions
	Plasma Composition	50% N+ / 50% H+ <m> 7.5 amu
	Plasma Speed (relative to Triton)	43 km/s
	Local Magnetic Field Strength	5 – 8 nT
	Alfven Speed	125-200 km/s
	N <sup>+</sup> Gyroradius at Triton	598 – 1315 km

1190  
1191 **Table A2:** List of the error sources included in the Monte Carlo simulation. Plasma interaction fields details are described further in Liuzzo et al. 2021.

1192



1193

1194

1195 **Figure A1:** Relative amplitude and phase delay of the ionosphere-only and ocean-plus-ionosphere models used in  
 1196 our study, plotted as a function of ionosphere HIC for both the (left panels) 14-hr synodic and the (right panels)  
 1197 141-hr orbital periods. Note that although the discriminability between the ionosphere-only models and the least-  
 1198 favorable likely ocean models in the amplitude response of the orbital wave is low and almost non-existent for the  
 1199 amplitude response of the synodic wave, the phase delay, especially at the 141-hr period, provides the differences in  
 1200 response needed to facilitate robust classification between the two model classes for the full range of ionosphere  
 1201 HICs used in the study.

1202

1203

## References

- 1204 Alken, P., Maute, A., Richmond, A., Vanhamäki, H., and Egbert, G., 2017. An application of  
 1205 principal component analysis to the interpretation of ionospheric current systems, *Journal of*  
 1206 *Geophysical Research: Space Physics*, vol. 122, pp. 5687-5708.
- 1207 Archinal, B.A., Acton, C. H., Hearn, M. F. A., et al., 2018. Report of the IAU Working Group  
 1208 on Cartographic Coordinates and Rotational Elements: 2015, *Celest Mech Dyn Astr* (2018)  
 1209 130:22, doi.org/10.1007/s10569-017-9805-5.
- 1210 Arridge, C. S., Eggington, J. W. B., 2021. Electromagnetic induction in the icy satellites of  
 1211 Uranus, *Icarus*, Volume 367, October 2021, 114562. doi.org/10.1016/j.icarus.2021.114562
- 1212 Castillo-Rogez J., Daswani, M. M., Glein C., Vance, S., Cochrane, C.J. 2021. Role of Non-  
 1213 Water Ices in Driving Ocean Salinity and Electrical Conductivity in Ocean Worlds.  
 1214 Submitted to *JGL*, 10.1002/essoar.10509076.1.
- 1215 Cochrane, C. J., Vance, S., Nordheim, T., et al., 2021. In search of Subsurface Oceans within the  
 1216 Moons of Uranus, *JGR Planets*, Volume 126, Issue 12, December 2021, e2021JE006956.  
 1217 doi.org/10.1029/2021JE006956
- 1218 Connerney, J., Acuna, M. H., and Ness, N. F., 1991. The magnetic field of Neptune, *Journal of*

- 1219 Geophysical Research: Space Physics, vol. 96, pp. 19023-19042.  
 1220 Croft, S.K., Soderblom, L.A., 1991. Geology of the Uranian satellites, in: Bergstrahl, J.T. (Ed.),  
 1221      Uranus. University of Arizona Press, Tucson, AZ, pp. 561–628.  
 1222 D. H. Eckhardt, "Geomagnetic Induction in a Concentrically Stratified Earth," Journal of  
 1223      Geophysical Research, vol. 68, p. 6273, 1963.  
 1224      <https://ui.adsabs.harvard.edu/abs/1963JGR....68.6273E>  
 1225 Croft, S., Kargel, J., Kirk, R. L., Moore, J., Schenk, P., and Strom, R., 1995. The geology of  
 1226      Triton, in Neptune and Triton, pp. 879-947.  
 1227 Grundy, W., Young, L., Stansberry, J., Buie, M., Olkin, C., and Young, E., 2010. Near-infrared  
 1228      spectral monitoring of Triton with IRTF/SpeX II: Spatial distribution and evolution of ices,  
 1229      Icarus, vol. 205, pp. 594-604.  
 1230 Grundy, W., and Young, L., 2004. Near-infrared spectral monitoring of Triton with IRTF/SpeX  
 1231      I: establishing a baseline for rotational variability, Icarus, vol. 172, pp. 455-465.  
 1232 Hansen, C. J., Castillo-Rogez, J., Grundy, W., et al., 2021. Triton: Fascinating Moon, Likely  
 1233      Ocean World, Compelling Destination! Planet. Sci. J. 2 137.  
 1234 Hartkorn, O., & Saur, J. (2017). Induction signals from Callisto's ionosphere and their  
 1235      implications on a possible subsurface ocean. Journal of Geophysical Research: Space  
 1236      Physics, 122(11), 11-677.  
 1237 Hendrix, A. R., Hurford, T. A., Barge, L. M., Bland, M. T., Bowman, J. S., Brinckerhoff, W.,  
 1238      Buratti, B. J., Cable, M. L., Castillo-Rogez, J., and Collins, G. C., 2019. The NASA  
 1239      Roadmap to Ocean Worlds, Astrobiology, vol. 19, pp. 1-27.  
 1240 Holler, B. J., Young, L. A., Grundy, W. M., and Olkin, C. B., 2015. Composition and evolution  
 1241      of Triton's icy surface between 2002-2014 from SpeX/IRTF, in AAS/Division for Planetary  
 1242      Sciences Meeting Abstracts 47, 2015.  
 1243 Hannachi, A., Jolliffe, I., and Stephenson, D., 2007. Empirical orthogonal functions and related  
 1244      techniques in atmospheric science: A review, International Journal of Climatology: A  
 1245      Journal of the Royal Meteorological Society, vol. 27, pp. 1119-1152.  
 1246 Hubbard, W.B., Podolak, M., Stevenson, D. J., 1995. Interior of Neptune, D. Cruickshank (Ed.),  
 1247      Neptune and Triton, Univ. of Arizona Press, Tucson, pp. 109-138  
 1248 Ip, W. H., 1990. On the ionosphere of Triton: An evaluation of the magnetospheric electron  
 1249      precipitation and photoionization effects, Geophysical Research Letters, vol. 17, pp. 1713-  
 1250      1716.  
 1251 Ivanov, M., and Borozdin, V., 1991. Enigmatic Circular Features in the Cantaloupe Terrain on  
 1252      Triton," in Lunar and Planetary Science Conference.  
 1253 Jolliffe, I. T., and Cadima, J., 2016. Principal component analysis: a review and recent  
 1254      developments, Philosophical Transactions of the Royal Society A: Mathematical, Physical  
 1255      and Engineering Sciences, vol. 374, p. 20150202.  
 1256      <https://royalsocietypublishing.org/doi/abs/10.1098/rsta.2015.0202> .  
 1257 Khurana, K. K., Kivelson, M. G., et al., 1998. Induced magnetic fields as evidence for subsurface  
 1258      oceans in Europa and Callisto, Nature 395 (6704) , pp.777-780.  
 1259 Kirk, R. L., Soderblom, L. A., Brown, R., Kieffer, S., and Kargel, J., 1995. Triton's plumes:  
 1260      discovery, characteristics, and models, in Neptune and Triton, pp. 949-989.  
 1261 Kivelson, M.G., Khurana, K.K., Stevenson, D.J., Bennett, L., Joy, S., Russell, C.T., Walker, R.J.,  
 1262      Zimmer, C., Polanskey, C., 1999. Europa and Callisto: Induced or intrinsic fields in a  
 1263      periodically varying plasma environment. J. Geophys. Res. Sp. Phys. 104, 4609–4625.  
 1264      <https://doi.org/10.1029/1998JA900095>

- 1265 Lamy L., 2020. Auroral emissions from Uranus and Neptune. *Phil. Trans. R. Soc.*,  
 1266 A.3782019048120190481  
 1267 <http://doi.org/10.1098/rsta.2019.0481>
- 1268 Liuzzo, L., Paty, C., Cochrane, C., Nordheim, T., Luspay-Kuti, A., Castillo-Rogez, J., Mandt, K.,  
 1269 Mitchell, K., Holmström, M., Addison, P., Simon, S., Poppe, A. R., Vance, S., and Prockter,  
 1270 L. (2021), Triton's Variable Interaction with Neptune's Magnetospheric Plasma, *Journal of*  
 1271 *Geophysical Research: Space Physics*, 126, e2021JA029740.
- 1272 Liuzzo, L., Simon, S., Feyerabend, M., & Motschmann, U. (2016). Disentangling plasma  
 1273 interaction and induction signatures at Callisto: The Galileo C10 flyby. *Journal of*  
 1274 *Geophysical Research: Space Physics*, 121(9), 8677-8694.
- 1275 Liuzzo, L., Simon, S., Feyerabend, M., & Motschmann, U. (2017). Magnetic signatures of  
 1276 plasma interaction and induction at Callisto: The Galileo C21, C22, C23, and C30 flybys.  
 1277 *Journal of Geophysical Research: Space Physics*, 122(7), 7364-7386.
- 1278 Liuzzo, L., Simon, S., & Feyerabend, M. (2018). Observability of Callisto's inductive signature  
 1279 during the JUpiter ICy moons Explorer mission. *Journal of Geophysical Research: Space*  
 1280 *Physics*, 123(11), 9045-9054.
- 1281 Kivelson, M.G., Khurana, K.K., Stevenson, D.J., Bennett, L., Joy, S., Russell, C.T., Walker, R.J.,  
 1282 Zimmer, C., Polanskey, C., 1999. Europa and Callisto: Induced or intrinsic fields in a  
 1283 periodically varying plasma environment. *J. Geophys. Res. Sp. Phys.* 104, 4609–4625.  
 1284 <https://doi.org/10.1029/1998JA900095>
- 1285 Kivelson, M.G., Khurana, K.K., Volwerk, M., 2002. The permanent and inductive magnetic  
 1286 moments of Ganymede. *Icarus* 157, 507–522. <https://doi.org/10.1006/icar.2002.6834>
- 1287 Mandt, K. E., and Luspay-Kuti, A., 2019. Comparative planetology of the ion chemistry  
 1288 and Pluto, Titan and Triton. *Pluto System After New Horizons*, LPI Contributions, vol.  
 1289 2133.
- 1290 Mejnertsen, L., Eastwood, J. P., Chittenden, J. P., & Masters, A. (2016). Global MHD  
 1291 simulations of Neptune's magnetosphere. *Journal of Geophysical Research: Space Physics*,  
 1292 121(8), 7497-7513.
- 1293 Müller, J., Simon, S., Motschmann, U., Schüle, J., Glassmeier, K. H., & Pringle, G. J. (2011).  
 1294 AIKEF: Adaptive hybrid model for space plasma simulations. *Computer Physics*  
 1295 *Communications*, 182(4), 946-966.
- 1296 Nimmo, F., Spencer, J. R., Pappalardo, R. T. and Mullen, M. E. (2007). Nature volume 447,  
 1297 pages 289–291.
- 1298 Nimmo, F., Spencer, J. R. (2015) Powering Triton's recent geological activity by obliquity tides:  
 1299 Implications for Pluto geology, *Icarus* 246, 2-10.
- 1300 Neubauer, F. M. (1980). Nonlinear standing Alfvén wave current system at Io: Theory. *Journal*  
 1301 *of Geophysical Research: Space Physics*, 85(A3), 1171-1178.
- 1302 Podolak, M., Weizman, A., Marley, M., 1995. Comparative models of Uranus and Neptune,  
 1303 *Planet. Space Sci.*, 43 (12), pp. 1517-1522
- 1304 Porco, C. C., Helfenstein, P., Thomas, P. C., et al., 2006. Cassini Observes the Active South Pole  
 1305 of Enceladus, *Science*, Vol. 311, Issue 5766, pp. 1393-1401. DOI: 10.1126/science.1123013
- 1306 Prockter, L. and Schenk, P., 2005. Origin and evolution of Castalia Macula, an anomalous young  
 1307 depression on Europa, *Icarus*, vol. 177, pp. 305-326.
- 1308 Rebello, L. R. R., Siepman, T., Drexler, S. (2020) Correlations between TDS and electrical  
 1309 conductivity for high-salinity formation brines characteristic of South Atlantic pre-salt  
 1310 basins, *Water SA* 46, 602-609, <https://doi.org/10.17159/wsa/2020.v46.i4.9073>

- 1311 Ruzmaikin, A. A., Starchenko, S. V., 1991. On the origin of Uranus and Neptune magnetic  
 1312 fields, *Icarus*, 93, pp. 82-87
- 1313 Saur, J., Neubauer, F. M., & Glassmeier, K. H. (2010). Induced magnetic fields in solar system  
 1314 bodies. *Space science reviews*, 152(1), 391-421
- 1315 Saur, J., Duling, S., Roth, L., Jia, X., 2015. The search for a subsurface ocean in Ganymede with  
 1316 Hubble Space Telescope observations of its auroral ovals, *JGR Space Physics*, Vol. 120,  
 1317 Issue 3, pp: 1715-1737. DOI10.1002/2014JA020778
- 1318 Schenk, P. M., and Zahnle, K., 2007. On the negligible surface age of Triton, *Icarus*, vol. 192,  
 1319 pp. 135-149.
- 1320 Schenk, P. M., 2008. Cartographic and topographic mapping of the icy satellites of the outer  
 1321 solar system, *ISPRS XXXVII*, Commission IV, WG IV/7.
- 1322 Schenk, P. M., and Jackson, M., 1993. Diapirism on Triton: A record of crustal layering and  
 1323 instability, *Geology*, vol. 21, pp. 299- 302.
- 1324 Schenk, P.M., Moore, J.M., Schenk, P.M., 2020. Topography and geology of Uranian mid-sized  
 1325 icy satellites in comparison with Saturnian and Plutonian satellites Subject Areas : Author  
 1326 for correspondence : <https://doi.org/10.1098/rsta.2020.0102>
- 1327 Schilling, N., Khurana, K.K., Kivelson, M.G., 2004. Limits on an intrinsic dipole moment in  
 1328 Europa. *J. Geophys. Res.* 109, doi:10.1029/2003JE002166, E05006.
- 1329 Soderlund K. M. and Stanley S. 2020. The underexplored frontier of ice giant dynamos. *Phil.  
 1330 Trans. R. Soc. A*.3782019047920190479, <http://doi.org/10.1098/rsta.2019.0479>
- 1331 Stanley, S., Bloxham, J., 2004. Convective-region geometry as the cause of Uranus' and  
 1332 Neptune's unusual magnetic field, *Nature*, 428, pp. 151-153
- 1333 Stanley, S., Bloxham, J., 2006. Numerical dynamo models of Uranus' and Neptune's magnetic  
 1334 fields, *Icarus*, Volume 184, Issue 2, Pages 556-572, ISSN 0019-1035
- 1335 Sittler, E. and Hartle, R., 1996. Triton's ionospheric source: Electron precipitation or  
 1336 photoionization, *Journal of Geophysical Research: Space Physics*, vol. 101, pp. 10863-  
 1337 10876.
- 1338 Srivastava, S. P. (1966). Theory of the magnetotelluric method for a spherical conductor.  
 1339 *Geophysical Journal International*, 11(4):373–387.
- 1340 Strobel, D. F., Simmers, M. E., Herbert, F., and Sandel, B. R., 1990. The photochemistry of  
 1341 methane in the atmosphere of Triton, *Geophysical Research Letters*, vol. 17, pp. 1729-1732.
- 1342 Tyler, G., Sweetnam, D., Anderson, J., Borutzki, S., Campbell, J., Eshleman, V., Gresh, D.,  
 1343 Gurrola, E., Hinson, D., and Kawashima, N., 1989. Voyager radio science observations of  
 1344 Neptune and Triton, *Science*, vol. 246, pp. 1466-1473.
- 1345 Vance, S. D., Styczinski, M. J., Bills, B. G., Cochrane, C. J., Soderlund, K. M., Gómez-Pérez,  
 1346 N., & Paty, C. (2021). Magnetic induction responses of Jupiter's ocean moons including  
 1347 effects from adiabatic convection. *Journal of Geophysical Research: Planets*, 126,  
 1348 e2020JE006418. 10.1029/2020JE006418
- 1349 Weiss, B. P., Biersteker, J. B., Colicci, V., Goode, A., Castillo-Rogez, J. C., Petropoulos, A. E., Balint & T. S.  
 1350 (2021b) Searching for subsurface oceans on the moons of Uranus using magnetic induction,  
 1351 *Geophysical Research Letters*, 48, e2021GL094758. <https://doi.org/10.1029/2021GL094758>
- 1352 Yung, Y., and Lyons, J., 1990. Triton: Topside ionosphere and nitrogen escape, *Geophysical  
 1353 research letters*, vol. 17, pp. 1717- 1720.
- 1354 Zhang, M., Richardson, J. D., & Sittler Jr, E. C. (1991). Voyager 2 electron observations in the  
 1355 magnetosphere of Neptune. *Journal of Geophysical Research: Space Physics*, 96(S01),  
 1356 19085-19100.
- 1357 Zimmer, C., Khurana, K.K., Kivelson, M.G., 2000. Subsurface Oceans on Europa and Callisto:

1358 Constraints from Galileo Magnetometer Observations”, Icarus, 147, 329–347.  
1359  
1360